LETTER

doi:10.1038/nature16534

Sub-particle reaction and photocurrent mapping to optimize catalyst-modified photoanodes

Justin B. Sambur[1], Tai-Yen Chen[1], Eric Choudhary[1]†, Guanqun Chen[1], Erin J. Nissen[2], Elayne M. Thomas[3], Ningmu Zou[1] & Peng Chen[1]

The splitting of water photoelectrochemically into hydrogen and oxygen represents a promising technology for converting solar energy to fuel[1,2]. The main challenge is to ensure that photogenerated holes efficiently oxidize water, which generally requires modification of the photoanode with an oxygen evolution catalyst (OEC) to increase the photocurrent and reduce the onset potential[3]. However, because excess OEC material can hinder light absorption and decrease photoanode performance[4], its deposition needs to be carefully controlled—yet it is unclear which semiconductor surface sites give optimal improvement if targeted for OEC deposition, and whether sites catalysing water oxidation also contribute to competing charge-carrier recombination with photogenerated electrons[5]. Surface heterogeneity[6] exacerbates these uncertainties, especially for nanostructured photoanodes benefiting from small charge-carrier transport distances[1,7,8]. Here we use super-resolution imaging[9–13], operated in a charge-carrier-selective manner and with a spatiotemporal resolution of approximately 30 nanometres and 15 milliseconds, to map both the electron- and hole-driven photoelectrocatalytic activities on single titanium oxide nanorods. We then map, with sub-particle resolution (about 390 nanometres), the photocurrent associated with water oxidation, and find that the most active sites for water oxidation are also the most important sites for charge-carrier recombination. Site-selective deposition of an OEC, guided by the activity maps, improves the overall performance of a given nanorod—even though more improvement in photocurrent efficiency correlates with less reduction in onset potential (and vice versa) at the sub-particle level. Moreover, the optimal catalyst deposition sites for photocurrent enhancement are the lower-activity sites, and for onset potential reduction the optimal sites are the sites with more positive onset potential, contrary to what is obtainable under typical deposition conditions. These findings allow us to suggest an activity-based strategy for rationally engineering catalyst-improved photoelectrodes, which should be widely applicable because our measurements can be performed for many different semiconductor and catalyst materials.

Single-crystalline rutile titanium oxide (TiO_2) nanorods (each of width 127 ± 27 nm and length $1{,}735 \pm 437$ nm) with defined surface facet orientations[14], known to be stable photoanodes for water oxidation[2], were dispersed on an indium-doped tin oxide (ITO) electrode in a microfluidic photoelectrochemical cell (Fig. 1a). To map the surface reactions of photogenerated holes and electrons on individual nanorods, we used single-molecule fluorescence microscopy[9–12] of either photogenerated hole (h^+)-induced amplex red oxidation or electron (e^-)-induced resazurin reduction (Extended Data Fig. 1) that both produce the fluorescent product resorufin as shown by ensemble photo (electro)catalysis measurements (Extended Data Figs 2, 3). In a typical experiment, the ITO electrode potential (E, referenced to the Ag/AgCl electrode) was fixed while a N_2-purged pH 8.3 electrolyte solution containing nanomolar nonfluorescent probe molecules flowed through the cell. Continuous 375-nm laser illumination generated charge-carriers within the TiO_2 nanorods, inducing a potential-dependent steady-state anodic photocurrent (i_{ss}, Fig. 1n, blue circles) from water oxidation[2]; the low probe concentration contributes insignificantly to i_{ss}. Another 532-nm laser induced the fluorescence of product molecules formed on nanorod surfaces. Anodic photocurrent and appreciable probe reactions were observed only with 375-nm laser illumination (Extended Data Figs 4a, 3c and 3e). Imaging and localizing individual resorufin molecules at a precision of about 30 nm (see Methods) maps the positions of hole- or electron-induced reactions across a range of potentials on each nanorod relative to its scanning electron microscope (SEM) image (Fig. 1b–g).

At potentials where i_{ss} is large ($E \geq -0.3$ V, Fig. 1n), hole-induced surface reaction rates are high but strikingly non-uniform along single nanorods (Fig. 1b, d, f), even though identical {100} facets span the length of each nanorod[14]. For 25 out of 37 nanorods, hole-induced reactions predominantly occur in one or a few nanometre-scale 'hotspots' (areas on a single nanorod denoting high hole activity) (Fig. 1b, d), while the remaining surface is less active. The smallest hotspots, of ~50 nm (Extended Data Fig. 5b, c), are much smaller than the diffraction-limited resolution of ~300 nm of our microscopic set-up, but are observable owing to super-resolution (that is, better than diffraction-limited optical resolution) as in earlier catalysis imaging studies[9]. For the remaining 12 out of the 37 nanorods studied, hole-induced reactions are distributed more evenly along the nanorods (Fig. 1f). At potentials where the anodic i_{ss} is minimal ($E \leq -0.4$ V, Fig. 1n), the electron-induced reaction rates are high and also occur non-uniformly along the nanorods (Fig. 1c, e, g). We note that intra-facet heterogeneity in the photocatalytic activity of TiO_2 crystals has also been observed in earlier studies[11,12].

The non-uniform distribution of reaction rates, and hence activity, indicates that the active site distribution differs among nanorods, and that the higher-activity sites are not {100} facet sites but instead probably the surface structural defects that we can discern using electron microscopy or the impurity atoms we detect in our elemental analysis (Extended Data Fig. 6). The reconstructed rutile {100} surface contains oxygen vacancies and small Ti_2O_3 units, which could act as catalytic units for water oxidation[15]. Of the impurities present in our system, Fe has been identified as a dopant that increases both photocatalytic reduction and oxidation activity of TiO_2 nanoparticles[16].

Surprisingly, our data indicate a strong spatial correlation between hole- and electron-induced activities (Fig. 1k): locations with high (or low) hole-induced activity at more positive potentials also exhibit high (or low) electron-induced activity at more negative potentials (see Fig. 1b versus Fig. 1c). The average separation between correlated hole- and electron-reaction hotspots on the same nanorod is ~40 nm (Extended Data Fig. 5d), comparable to our localization precision. This spatial correlation is unlikely to arise from preferential probe

---

[1]Department of Chemistry and Chemical Biology, Cornell University, Ithaca, New York 14853, USA. [2]Department of Chemistry, Colorado Mesa University, Grand Junction, Colorado 81501, USA. [3]Department of Materials Science and Engineering, University of Michigan, Ann Arbor, Michigan 48109, USA. †Present address: Center for Nanoscience and Technology, NIST, Gaithersburg, Maryland 20899, USA.

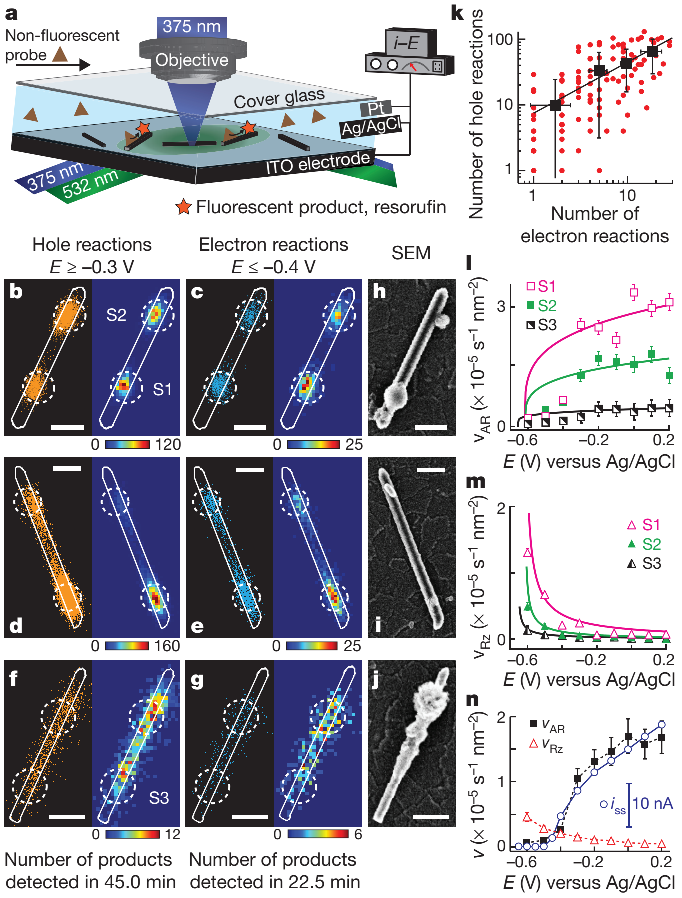

Figure 1 | Super-resolution hole and electron surface reaction mapping. **a**, Experimental setup for wide-field single-molecule fluorescence imaging of photoelectrocatalysis via two-laser total internal reflection excitation, or for sub-nanorod photocurrent measurements via focused laser excitation, in a three-electrode microfluidic photoelectrochemical cell (Methods). **b**, Scatter plot (left) and two-dimensional histogram ($40 \times 40\,\text{nm}^2$ pixels; right) of all individual resorufin product molecules (orange dots) generated from hole-induced amplex red oxidation reactions at $E \geq -0.3$ V on a single TiO_2 nanorod with two localized hotspots. The solid white line is the outline of the nanorod, determined using SEM. Dashed white circles denote focused 375-nm laser spots for photocurrent measurements and OEC deposition. The colour scales indicate number of products formed. **c**, Same as **b**, but at $E \leq -0.4$ V, and the blue dots are resorufin product molecules generated from electron-induced resazurin reduction reactions. **d**–**g**, Same as **b** and **c**, but for a nanorod with a single dominant hole reaction hotspot (**d**, **e**) or delocalized hole reactions (**f**, **g**). **h**–**j**, SEM images of the three nanorods in **b**–**g** after OEC deposition. All scale bars are 400 nm. **k**, Pixel-to-pixel correlation (red dots) between the two-dimensional histograms of hole and electron surface reactions, respectively, in **b** and **c** for the whole nanorod with a cross-correlation coefficient of $\rho = 0.84 \pm 0.01$. Black squares represent the binned and averaged data to obtain the general trend; the black line is the linear fit. **l** and **m**, Potential dependences of v_{AR} and v_{Rz} at spots S1, S2 and S3 on the nanorods in **b**, **c**, **f** and **g**. Solid lines are global fits with equation (2) (for $E > -0.4$ V) and equation (3). **n**, Comparison of i_{ss} from ~1,000 TiO_2 nanorods and nanorod-averaged v_{AR} and v_{Rz} for 78 spots from 37 nanorods. All error bars represent s.d.

adsorption to the same surface sites, given that controls show the structurally similar product (Extended Data Fig. 1a) adsorbs equivalently to all surface sites (Extended Data Fig. 7). We note that although it has been shown that photogenerated holes and electrons can preferentially react at the same facet of semiconductor microcrystal photocatalysts[17], our data further indicate that holes and electrons tend to reach and react at the same surface sites within a given nanorod facet.

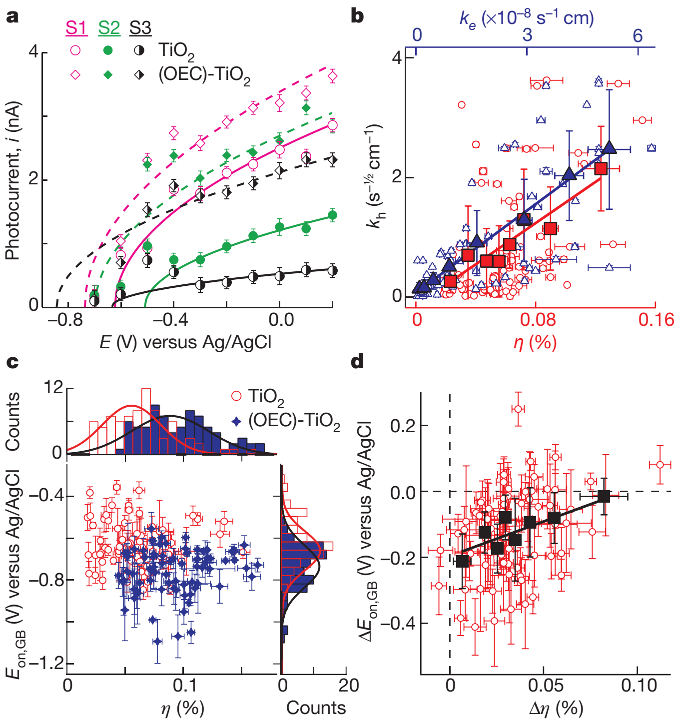

Figure 2 | Correlation between local *i*–*E* responses, surface activities, and OEC effects. **a**, *i*–*E* curves from spots S1, S2 and S3 in Fig. 1b, c, f and g before and after OEC deposition. Lines are fits using equation (1). **b**, Correlation of k_h with η and with k_e for the same 78 spots (open symbols), with cross-correlation coefficients $\rho(k_h, \eta) = 0.45 \pm 0.06$ and $\rho(k_h, k_e) = 0.75 \pm 0.03$. Solid symbols are binned and averaged data to obtain general trends; lines are linear fits. **c**, $E_{on,GB}$ versus η for 78 nanorod spots before and after OEC deposition. Top and right, histograms of η and $E_{on,GB}$. Counts are the number of nanorod spots. Lines are Gaussian fits, giving: $\eta = 0.056 \pm 0.023\%$ and $E_{on,GB} = -0.66 \pm 0.09$ V for TiO_2 and $\eta_{OEC} = 0.088 \pm 0.033\%$ and $E_{on,GB,OEC} = -0.73 \pm 0.10$ V for (OEC)-TiO_2. **d**, Correlation between $\Delta E_{on,GB} = E_{on,GB,OEC} - E_{on,GB}$ and $\Delta\eta = \eta_{OEC} - \eta$ for 78 spots (red circles). Black squares are data binned and averaged to obtain the general trend; the black line is the linear fit. Error bars for individual nanorod spots represent s.d. and error bars for binned and averaged data represent s.e.m.

At any location on a nanorod, whether a hotspot (see S1 in Fig. 1b) or a low-activity spot (see S3 in Fig. 1f), the hole-induced amplex red oxidation rate (v_{AR}) becomes clearly noticeable at about −0.5 V (Fig. 1l), commensurate with the steady-state photocurrent i_{ss} and its onset potential ($E_{on,ss}$) of −0.47 V (Fig. 1n). We find that v_{AR} scales with $E^{1/4}$ for $E \geq -0.3$ V (Extended Data Fig. 3b) and with $I_0^{1/2}$ when using a fixed positive potential ($I_0 = 375$ nm laser power; Extended Data Fig. 3c), consistent with amplex red reacting with surface-adsorbed $OH^{\bullet}$ radicals produced from hole-induced oxidation of OH^- or H_2O (ref. 18). The electron-induced resazurin reduction rate (v_{Rz}) shows an opposite trend: v_{Rz} is high at $E < E_{on,ss}$ (Fig. 1m) and decreases greatly at $E > E_{on,ss}$, where a ~0.02-nA (~10^8 holes per second) anodic photocurrent is measured per nanorod (Fig. 1n). The measurable v_{Rz} at $E > E_{on,ss}$ indicates that even under highly anodic conditions, single-molecule fluorescence microscopy is able to detect the photogenerated electrons that escape being collected by the ITO electrode and participate instead in surface reactions (that is, surface recombination).

To assess local water oxidation efficiencies, we focused a 375-nm laser (focus diameter ~390 nm) onto a nanorod spot and measured potential-dependent photocurrents through the ITO electrode (Fig. 1a). Different *i*–*E* responses measured for different spots on the same nanorod (such as S1 versus S2 in Fig. 2a) suggest that we are indeed measuring local, sub-nanorod photoelectrochemical behaviour. We find that the anodic photocurrent *i* always scales with $(E)^{1/2}$

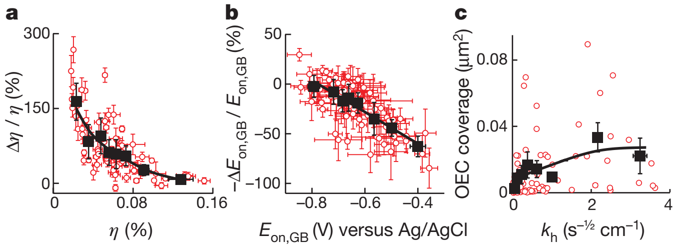

Figure 3 | η and $E_{on,GB}$ changes of OEC-modified TiO_2 nanorods. **a**, Relative change in absorbed-photon-to-current efficiency ($\Delta\eta/\eta$) versus initial η for 78 nanorod spots (open circles). **b**, Relative change in onset potential ($-\Delta E_{on,GB}/E_{on,GB}$) versus initial $E_{on,GB}$ (open circles), where negative values represent negative shifts in $E_{on,GB}$. **c**, Catalyst coverage (Methods) versus k_h. Black squares show binned and averaged data; black lines are spline interpolations. Error bars for individual nanorod spots represent s.d. and error bars for binned and averaged data represent s.e.m.

for $E \geq -0.3$ V (Extended Data Fig. 8d); for $E < -0.3$ V and especially near $E_{on,ss}$ (−0.47 V), it deviates from the $(E)^{1/2}$ dependence owing to photocurrent transient dynamics (Extended Data Fig. 4b)[19]. At fixed positive potentials, the photocurrent scales linearly with I_0 (Extended Data Fig. 4c). Spots with higher hole and electron activities (such as spot S1) show larger photocurrents, indicating that higher surface activity is related to higher water oxidation efficiency.

To relate local water oxidation efficiency to surface hole and electron activities, we use the Gärtner–Butler[20,21] and Reichman[22] models to analyse quantitatively the i–E, ν_{AR}–E, and ν_{Rz}–E data from 78 nanorod spots (equations (1) to (3) in the Methods). For each spot, this yields η (the absorbed-photon-to-current efficiency within the depletion layer of the nanorod), $E_{on,GB}$ (the photocurrent onset potential predicted by the Gärtner–Butler model) and the effective rate constants k_h and k_e that represent hole and electron surface activities, respectively. Spots with larger η have larger k_h (Fig. 2b), as expected from the association between water oxidation efficiency and surface hole activity, with both terms including the efficiencies of hole transport to the surface and interfacial charge transfer[23]. The k_h value for each spot is also strongly correlated with its k_e value, further supporting the idea that photogenerated holes and electrons prefer to reach and react at the same sites. Importantly, the strong correlation between η and surface hole and electron activities suggests that the nanorod sites exhibiting higher water oxidation efficiency effectively mediate both oxidation and reduction reactions (the dominant process depends on the applied potential), making them also more effective surface recombination sites than the lower efficiency sites. This dual oxidation–reduction activity is consistent with the earlier observation that both oxidative and reductive photocatalytic reactions preferentially occur on the same {100} facets on $SrTiO_3$ crystals[17]. We hypothesize that this dual activity might make it easier for high-efficiency sites to accept photogenerated holes from the semiconductor interior and transfer them to adsorbed OH^- or H_2O (that is, the sites are oxidized and reduced sequentially in a redox cycle, illustrated in Supplementary Scheme 1).

In a next step, we photoelectrochemically deposited the OEC cobalt-borate (Co-B$_i$) site-selectively by focusing a 375-nm laser onto either high- or low-activity spots where i–E data had been measured. This resulted in heterogeneous OEC coverage (Fig. 1h–j) and enhanced photocurrents in subsequent i–E measurements (Fig. 2a), as expected for this amorphous catalyst[24,25], with the enhancement saturating[26] as increasing catalyst is deposited (Extended Data Fig. 9b). Gärtner–Butler model analysis shows that OEC deposition increases the value of η for nearly all nanorod spots (that is, $\Delta\eta > 0$, Fig. 2d), on average by ~60% (Fig. 2c, top). OEC deposition also induced an average shift in $E_{on,GB}$ of −70 mV (Fig. 2c, right), as expected from the reduced overpotential seen in OEC-modified photoanodes[27], but surprisingly 16% of spots exhibited positive shifts (that is, $\Delta E_{on,GB} > 0$; Fig. 2d). For spots exhibiting the expected $\Delta E_{on,GB} < 0$ V, the magnitude of $\Delta E_{on,GB}$ is smaller for spots with larger $\Delta\eta$ (Fig. 2d). We conclude that photocurrent enhancements from OEC deposition on these nanorods are not necessarily accompanied by negative shifts in $E_{on,GB}$, and that the magnitudes of their changes can be anticorrelated.

The most striking effects of OEC deposition are changes in η and $E_{on,GB}$ compared with their initial values. A strong negative correlation exists for the relative change in η (that is, $\Delta\eta/\eta$, Fig. 3a): spots with smaller initial η, characterized also by lower surface hole and electron activities, experience larger relative enhancements that can exceed 200%. This trend could be partly due to larger gains in interfacial charge transfer efficiency for initially low-η spots, because OEC does not typically affect charge transport[26]. A strong negative correlation also exists between $\Delta E_{on,GB}/E_{on,GB}$ and $E_{on,GB}$ (Fig. 3b): spots with more positive initial $E_{on,GB}$ exhibit larger relative negative shifts in $E_{on,GB}$. We attribute this trend to the ability of the OEC to relieve excess positive surface charge[26,28] and that larger negative shifts in $E_{on,GB}$ are possible for sites with initially more excess surface charge[29].

OEC deposition sites that optimize photocurrent enhancement are thus those with the lowest hole and electron activities, while deposition sites that most reduce onset potentials are those with the most positive $E_{on,GB}$ values. These two types of sites are not necessarily the same (Fig. 2d), which highlights the challenge of trying to engineer photoanodes with a minimal amount of catalyst. First, under typical photoelectrodeposition (or photodeposition) conditions, more catalyst material is deposited onto higher-activity sites (Fig. 3c and refs 30, 31) that show less photocurrent enhancement. Second, upon scanning the potential positively, OEC deposition is expected to initiate earlier at sites with more negative $E_{on,GB}$. Both effects deposit more catalyst where it is least needed.

We propose to circumvent this problem with a block–deposit–remove strategy based on function rather than structure (Extended Data Fig. 10). This would involve first blocking sites with more negative $E_{on,GB}$ and higher η by photoelectrochemically depositing protecting groups at increasingly positive potentials; then depositing the desired catalyst at the remaining sites with more positive $E_{on,GB}$ or lower η; and, finally, removal of the blocking groups to yield a photoanode with optimally located catalysts.

Online Content Methods, along with any additional Extended Data display items and Source Data, are available in the online version of the paper; references unique to these sections appear only in the online paper.

Received 20 July; accepted 7 December 2015.

1. Walter, M. G. *et al.* Solar water splitting cells. *Chem. Rev.* **110,** 6446–6473 (2010).
2. Fujishima, A. & Honda, K. Electrochemical photolysis of water at a semiconductor electrode. *Nature* **238,** 37–38 (1972).
3. Yang, J., Wang, D., Han, H. & Li, C. Roles of cocatalysts in photocatalysis and photoelectrocatalysis. *Acc. Chem. Res.* **46,** 1900–1909 (2013).
4. Carroll, G., Zhong, D. & Gamelin, D. Mechanistic insights into solar water oxidation by cobalt-phosphate-modified α-Fe_2O_3 photoanodes. *Energy Environ. Sci.* **8,** 577–584 (2015).
5. Wilson, R. H. A model for the current-voltage curve of photoexcited semiconductor electrodes. *J. Appl. Phys.* **48,** 4292–4297 (1977).
6. Buurmans, I. L. C. & Weckhuysen, B. M. Heterogeneities of individual catalyst particles in space and time as monitored by spectroscopy. *Nature Chem.* **4,** 873–886 (2012).
7. Liu, C., Dasgupta, N. P. & Yang, P. Semiconductor nanowires for artificial photosynthesis. *Chem. Mater.* **26,** 415–422 (2014).
8. Warren, S. C. *et al.* Identifying champion nanostructures for solar water-splitting. *Nature Mater.* **12,** 842–849 (2013).
9. Roeffaers, M. B. J. *et al.* Super-resolution reactivity mapping of nanostructured catalyst particles. *Angew. Chem. Int. Ed.* **48,** 9285–9289 (2009).
10. Zhou, X. *et al.* Quantitative super-resolution imaging uncovers reactivity patterns on single nanocatalysts. *Nature Nanotechnol.* **7,** 237–241 (2012).
11. Zhang, Y. *et al.* Superresolution fluorescence mapping of single-nanoparticle catalysts reveals spatiotemporal variations in surface reactivity. *Proc. Natl Acad. Sci. USA* **112,** 8959–8964 (2015).
12. Tachikawa, T., Yamashita, S. & Majima, T. Evidence for crystal-face-dependent TiO_2 photocatalysis from single-molecule imaging and kinetic analysis. *J. Am. Chem. Soc.* **133,** 7197–7204 (2011).
13. Xu, W. *et al.* Single-molecule electrocatalysis by single-walled carbon nanotubes. *Nano Lett.* **9,** 3968–3973 (2009).

14. Liu, B. *et al.* Large-scale synthesis of transition-metal-doped TiO_2 nanowires with controllable overpotential. *J. Am. Chem. Soc.* **135,** 9995–9998 (2013).
15. Salvador, P., Garcia Gonzalez, M. L. & Munoz, F. Catalytic role of lattice defects in the photoassisted oxidation of water at (001) n-TiO_2 rutile. *J. Phys. Chem.* **96,** 10349–10353 (1992).
16. Choi, W., Termin, A. & Hoffmann, M. R. The role of metal ion dopants in quantum-sized TiO_2: correlation between photoreactivity and charge carrier recombination dynamics. *J. Phys. Chem.* **98,** 13669–13679 (1994).
17. Giocondi, J., Salvador, P. & Rohrer, G. The origin of photochemical anisotropy in $SrTiO_3$. *Top. Catal.* **44,** 529–533 (2007).
18. Villarreal, T. L., Gómez, R., Neumann-Spallart, M., Alonso-Vante, N. & Salvador, P. Semiconductor photooxidation of pollutants dissolved in water: a kinetic model for distinguishing between direct and indirect interfacial hole transfer. I. Photoelectrochemical experiments with polycrystalline anatase electrodes under current doubling and absence of recombination. *J. Phys. Chem. B* **108,** 15172–15181 (2004).
19. Salvador, P. Kinetic approach to the photocurrent transients in water photoelectrolysis at n-TiO_2 electrodes. 1. Analysis of the ratio of the instantaneous to steady-state photocurrent. *J. Phys. Chem.* **89,** 3863–3869 (1985).
20. Gärtner, W. W. Depletion-layer photoeffects in semiconductors. *Phys. Rev.* **116,** 84–87 (1959).
21. Butler, M. A. Photoelectrolysis and physical properties of the semiconducting electrode WO_3. *J. Appl. Phys.* **48,** 1914–1920 (1977).
22. Reichman, J. Collection efficiency of low-mobility solar cells. *Appl. Phys. Lett.* **38,** 251–253 (1981).
23. Dotan, H., Sivula, K., Gratzel, M., Rothschild, A. & Warren, S. C. Probing the photoelectrochemical properties of hematite (α-Fe_2O_3) electrodes using hydrogen peroxide as a hole scavenger. *Energy Environ. Sci.* **4,** 958–964 (2011).
24. Surendranath, Y., Lutterman, D. A., Liu, Y. & Nocera, D. G. Nucleation, growth, and repair of a cobalt-based oxygen evolving catalyst. *J. Am. Chem. Soc.* **134,** 6326–6336 (2012).
25. Khnayzer, R. S. *et al.* Structure and activity of photochemically deposited "CoPi" oxygen evolving catalyst on titania. *ACS Catal.* **2,** 2150–2160 (2012).
26. Klahr, B., Gimenez, S., Fabregat-Santiago, F., Bisquert, J. & Hamann, T. W. Photoelectrochemical and impedance spectroscopic investigation of water oxidation with "Co–Pi"-coated hematite electrodes. *J. Am. Chem. Soc.* **134,** 16693–16700 (2012).
27. Gamelin, D. R. Water splitting: catalyst or spectator? *Nature Chem.* **4,** 965–967 (2012).
28. Lin, F. & Boettcher, S. W. Adaptive semiconductor/electrocatalyst junctions in water-splitting photoanodes. *Nature Mater.* **13,** 81–86 (2013).
29. Peter, L. M., Li, J. & Peat, R. Surface recombination at semiconductor electrodes: Part I. Transient and steady-state photocurrents. *J. Electroanal. Chem. Interfacial Electrochem.* **165,** 29–40 (1984).
30. Steinmiller, E. M. P. & Choi, K. S. Photochemical deposition of cobalt-based oxygen evolving catalyst on a semiconductor photoanode for solar oxygen production. *Proc. Natl Acad. Sci. USA* **106,** 20633–20636 (2009).
31. Li, R. *et al.* Spatial separation of photogenerated electrons and holes among {010} and {110} crystal facets of $BiVO_4$. *Nature Commun.* **4,** 1432 (2013).

Supplementary Information is available in the online version of the paper.

Acknowledgements The research is supported by the Department of Energy, Office of Science, Basic Energy Science (grant number DE-FG02-10ER16199), and in part by Army Research Office (grant numbers 63767-CH and 65814-CH), National Science Foundation (grant numbers CBET-1263736 and CHE-1137217 (to J.B.S.), and REU programme DMR-1063059 (to E.J.N. and E.M.T.)), and the Petroleum Research Foundation (grant number 54289-ND7). This work used the Cornell Center for Materials Research Shared Facilities, an NSF MRSEC programme (grant number DMR-1120296), and the Cornell NanoScale Facility, a member of the NSF National Nanotechnology Infrastructure Network (grant number ECCS-15420819). We thank D. Hill of the Cahoon Group at the University of North Carolina at Chapel Hill for the finite-difference frequency-domain simulations presented in Supplementary Fig. 24. We also thank J. McKone, S. Maldonado, B. A. Parkinson, H. D. Abruña and A. J. Nozik for discussions, J. Colson and W. Dichtel for X-ray diffraction measurements, J. Grazul for electron microscopy and H. D. Abruña for electrochemical instrumentation.

Author Contributions J.B.S. and P.C. designed research. J.B.S. performed research. T.-Y.C., E.C., G.C., E.J.N., E.M.T. and N.Z. contributed to research. J.B.S. and P.C. analysed data and wrote the manuscript.

Author Information Reprints and permissions information is available at www.nature.com/reprints. The authors declare competing financial interests: details are available in the online version of the paper. Readers are welcome to comment on the online version of the paper. Correspondence and requests for materials should be addressed to P.C. (pc252@cornell.edu).

METHODS

Synthesis and characterization of TiO$_2$ nanorods. Single-crystalline rutile TiO$_2$ nanorods were synthesized via a molten-flux salt method following Liu *et al.*[14] and characterized by electron microscopy and X-ray diffraction. They have rectangular cross-sections with {100} side facets and {011} end facets. The ensemble-average diameter and length are 62 ± 16 nm and 263 ± 113 nm, respectively (Supplementary Fig. 1). The 37 nanorods on which we performed measurements have diameters of 127 ± 27 nm and lengths of 1,735 ± 437 nm.

Redox-selective fluorogenic probe reactions. The fluorogenic probe reaction was either oxidation of amplex red, a hole-probe, or reduction of resazurin, an electron-probe, both generating the fluorescent product resorufin (Extended Data Fig. 1a). Amplex red's oxidation potential is $\sim$2 V more negative than the valence band edge of TiO$_2$, and resazurin's reduction potential is $\sim$0.5 V more positive than the conduction band edge of TiO$_2$, determined from cyclic voltammetry (Extended Data Fig. 1b, c).

Single-molecule super-resolution imaging of surface reactions. A schematic illustration of the single-molecule super-resolution fluorescence microscopy experimental setup is shown in Fig. 1a, based on a wide-field prism-type total internal reflection fluorescence (TIRF) microscope as described previously[10]. TiO$_2$ nanorods were spin-coated onto an ITO electrode and annealed at 450 °C for 30 min, then assembled into an electrochemical microfluidic cell ($\sim$5 mm wide and 100 μm high) using double-sided tape sandwiched between an ITO electrode and a coverslip (Supplementary Fig. 3). A syringe pump drives the continuous supply of the reactant solution at 25 μl min^{-1}, which supplies 1×10^{10} probe molecules (at 50 nM) per second to the cell, whereas the maximum rate of product formation (or reactant consumption) from all of the nanorods in the flow cell was only 5×10^7 molecules per second, estimated from the amplex red oxidation reaction rate at +0.2 V and the fact that $\sim$2% of the 1.27-cm^2 ITO surface area was covered with nanorods. In all experiments, the electrolyte solution was deaerated 1 M KCl, 100 mM pH 8.3 sodium borate buffer. The deaeration via N$_2$-purging here removes O$_2$ from the cell, preventing both the competition for the photogenerated electrons by O$_2$ and the subsequent formation of O$_2^{\bullet -}$, which could oxidize amplex red[32]. All experiments were performed at room temperature.

A continuous wave circularly polarized 532-nm laser (630 W cm^{-2}) induces the fluorescence of the reaction product resorufin. The TiO$_2$ nanorods were also excited via TIRF illumination using a 375-nm laser (60 W cm^{-2}). The fluorescence was imaged by an electron multiplying charge coupled device (EMCCD) camera operated at a 15-ms frame rate. In a typical experiment, a sequence of fluorescence images (that is, 'catalytic movie') was acquired while the electrode potential, light intensity, flow rate and reactant concentration (either 50 nM amplex red or 50 nM resazurin) were fixed. Potential-dependent movies were acquired by stepping the potential in 0.1 V increments from −0.6 V to +0.2 V for amplex red oxidation experiments and from +0.2 V to −0.6 V for resazurin reduction experiments. The sequence of reactions were alternated (that is, amplex red imaging before resazurin imaging or vice versa for five different sample areas) and did not affect the results. The total acquisition time at each potential was 30,000 frames (that is, 7.5 min). As we only studied isolated nanorods, charge transport between adjacent nanorods does not apply to the photoelectrochemical processes measured.

The fluorescence images in the movies were analysed using a home-written MATLAB program, as described[33], to localize the positions of individual fluorescent products on single nanorods to $\sim$30 nm precision (Extended Data Fig. 5a), in correlation with the nanorod's SEM image (for example, Fig. 1b, left). These positions can then be histogrammed to generate an image at super-optical resolution (for example, Fig. 1b, right). Detailed data analysis procedures can be found in Supplementary Note 2.

There are other techniques also capable of measuring electrochemical or catalytic activities of single nano-entities (see review[34]), including scanning electrochemical (cell) microscopy[35–39], directly attaching a single particle to an ultramicroelectrode[38,40], electrocatalytic current amplification via single-nanoparticle collisions[41], surface plasmon resonance spectroscopy[42–44], and conventional optical microscopy[6,45].

Elemental analysis and high-resolution electron microscopy. The non-uniform hole and electron reaction rates along the single nanorods indicates that the higher-activity sites are most probably not the {100} facet sites. From the elemental and transmission electron microscopy (TEM) analysis (Extended Data Fig. 6), we hypothesize that these higher-activity sites are probably impurity atoms or surface structural defects.

For impurities, we have detected a number of impurity atoms in these nanorods via inductively coupled plasma atomic emission spectroscopy (ICP-AES, Extended Data Fig. 6a), among which Fe has been identified as a transition-metal dopant that increases both photocatalytic reduction and oxidation activity of TiO$_2$ nanoparticles[16]. Yang and co-workers[14], whose procedure we followed to synthesize these TiO$_2$ nanorods, intentionally doped these nanorods with 2% Fe, which resulted in a reduction in the overpotential for oxygen evolution on these nanorods, directly supporting our hypothesis. Elemental mapping of single nanorods further showed that some of these impurity atoms, including Fe, are heterogeneously distributed within a single nanorod (Extended Data Fig. 6b–f). There is also evidence in the literature that single impurity atoms can act as highly active catalytic sites on TiO$_2$ nanomaterials[46,47]. On the other hand, according to ref. 48, large impurity concentrations have an adverse effect on charge carrier transport: the mobility due to impurity scattering can theoretically be shown to vary as $\sim 1/N_{\mathrm{T}}$, where N_{T} is the total impurity concentration. Indeed, we measure smaller photocurrent efficiencies for larger-diameter nanorods (Supplementary Fig. 19b), for which the electrons have to travel longer distances to reach the ITO electrode.

For structural defects, high-resolution TEM shows that these nanorods have a structurally irregular surface layer (Extended Data Fig. 6g), even though the bulk of a nanorod is a single crystal (Extended Data Fig. 6h). There is also some indication of an irregular surface structure in the study by Liu *et al.*[14], whose synthesis procedure we followed. The irregular surface structure could be caused by surface reconstruction of the rutile {100} surface facets, which was previously observed for rutile {100} single-crystal surfaces annealed in the presence of O$_2$[49,50] (our nanorod sample was synthesized and annealed in air). The reconstructed surface is oxygen deficient (that is, oxygen vacancies are present) and contains small Ti$_2$O$_3$ units, which could behave as catalytic units for water oxidation[15].

The two probe molecules adsorb to all surface sites equivalently. To test whether our two structurally similar probe molecules amplex red and resazurin sample all surface sites in an unbiased way, we analysed the residence time of the reaction product resorufin (which is also structurally similar to amplex red and resazurin; Extended Data Fig. 1a) on the nanorod as a function of position. Using the three nanorods we presented as examples, we separate each nanorod into 150-nm segments (for example, Extended Data Fig. 7a, b, d, e, g and h), and within each segment we calculated the average residence time of the individual resorufin molecules; this average residence time is a good measure of how strongly resorufin, and presumably amplex red and resazurin, adsorb on the surface. Across the different segments within each nanorod, the average residence time of resorufin is essentially equivalent ($\sim$15 ms) and is independent of location (Extended Data Fig. 7c, f, i), even though different segments differ greatly in their reaction rates. This independence of location for the average residence time indicates that resorufin, and presumably amplex red and resazurin, adsorb equally on all surface sites along the side facets. We also determined the average residence times of resorufin from the 78 nanoscale spots where v_{AR}–E, v_{RZ}–E and i–E behaviours were analysed. The average product residence time is independent of the effective rate constants k_{h} and k_{e} (Extended Data Fig. 7j), further confirming that resorufin, and presumably amplex red and resazurin, do not preferentially adsorb onto higher- or lower-activity sites.

Ensemble photoelectrochemical measurements. Ensemble-level photoelectrochemical measurements were performed using a potentiostat connected to the three-electrode electrochemical microfluidic cell mounted on the optical microscope. Either a chopped 365-nm light-emitting diode (LED) or a 375-nm laser illuminated the sample. Two illumination conditions were used for the 375-nm laser excitation: (1) large illumination spot (1 × 1 cm^2) by removing the objective and (2) prism-type total internal reflection illumination with a small spot size of 80 × 95 μm^2, so as to access a large range of power density of a few milliwatts per square centimetre up to 0.2 kW cm^{-2}.

Sub-nanorod photocurrent measurements. A focused 375-nm laser was used to excite individual spots on individual nanorods in a front-side illumination geometry through the electrolyte (Fig. 1a), with a focus diameter of 392 nm (Supplementary Fig. 4) and maximal power density of 6.6 MW cm^{-2}. This spatially localized carrier excitation ensured that the photocurrent response stemmed from a particular nanorod, even though there were many other nanorods on the same ITO electrode. The 375-nm laser excitation light was chopped at 1 Hz and a lock-in amplifier was used to detect the nanoampere-level current from a single nanorod on top of the microampere-level background current of the ITO electrode via an analogue potentiostat (Supplementary Note 1.5). The i–E data of all individual nanorod spots were acquired in −0.1 V increments from +0.2 V to −0.7 V.

Quantitative analysis of i–E, v_{AR}–E and v_{Rz}–E data. We used a modified Gärtner–Butler model[20,21] to analyse the i–E data. This model assumes that the applied E is manifested entirely as a potential drop within the depletion layer of the semiconductor (that is, the depletion approximation), whose thickness W increases with $E^{1/2}$, and only charge carriers photogenerated within W contribute to the photocurrent.

Using a factor η as the absorbed-photon-to-current efficiency within W, we derived (Supplementary Note 3):

$$i=\eta qI_0\alpha\left(\frac{s}{S}\right)W=\eta qI_0\alpha\left(\frac{s}{S}\right)\sqrt{\frac{2\varepsilon\varepsilon_0(E-E_{\mathrm{on,GB}})}{qN_{\mathrm{d}}}} \tag{1}$$

This η contains contributions from both η_{sep}, the efficiency of charge carrier separation and transport to the collecting contact, and η_{surf}, the efficiency of charge transfer at the interface (Supplementary Note 5.3)[23]. q is the electronic charge, α is the absorption coefficient at 375 nm ($\alpha=10^4\,\mathrm{cm}^{-1}$)[51], s is the nanorod's geometric cross-section within the laser illumination area (S), ε is the dielectric constant of rutile $\mathrm{TiO_2}$ ($\varepsilon=100$)[52], ε_0 is the vacuum permittivity, and N_{d} is the doping density ($N_{\mathrm{d}}=10^{18}\,\mathrm{cm}^{-3}$; see Supplementary Note 3.6). $E_{\mathrm{on,GB}}$ is the photocurrent onset potential predicted by the Gärtner–Butler model (that is, when $E>E_{\mathrm{on,GB}}$, $i>0$). For an ideal semiconductor–electrolyte interface (so that the depletion approximation applies) with minimal light absorption in the depletion region and negligible photocurrent contribution from carriers outside the depletion region, this $E_{\mathrm{on,GB}}$ is equivalent to the flat band potential for the semiconductor (see Supplementary Note 3.5). Possible nano-optical effects on the absorption coefficient α of $\mathrm{TiO_2}$ nanorods as well as the changes caused by OEC deposition are considered in Supplementary Note 5.7; these effects do not affect any of our conclusions.

Equation (1) satisfactorily accounts for the dependence of i on I_0 and i on $E^{1/2}$ for $E\geq-0.3$ V before and after OEC deposition (Fig. 2a, Extended Data Figs 4a, c and 8b–d). Data fitting gives η and $E_{\mathrm{on,GB}}$ for each spot of each nanorod before and after OEC deposition (Fig. 2a). Data at $E\leq-0.4$ V were not fitted as they are complicated by photocurrent transient dynamics (Extended Data Fig. 4b).

The Gärtner–Butler model also allowed for treating the $E^{1/4}$ and $I_0^{1/2}$ dependences of v_{AR} by assuming that a primary step in water oxidation is hole transfer to surface-adsorbed $\mathrm{OH^-}$ or $\mathrm{H_2O}$ to generate $\mathrm{OH^{\bullet}}$ radicals[18,53] and incorporating that amplex red reacts with $\mathrm{OH^{\bullet}}$ radicals[11,32,54]. The v_{Rz}–E data could be treated by assuming that resazurin reacts with surface-accessible photogenerated electrons whose steady-state surface concentration is given by Reichman[22]. We derived (Supplementary Note 4):

$$v_{\mathrm{AR}}=k_h\sqrt{I_0\frac{\alpha}{A}\frac{s}{S}}\sqrt[4]{\frac{2\varepsilon\varepsilon_0(E-E_{\mathrm{on,GB}})}{qN_{\mathrm{d}}}} \tag{2}$$

$$v_{\mathrm{Rz}}=\frac{k_e(I_0/A)(s/S)}{\left(v_c+\mu_n\sqrt{\frac{2q}{\varepsilon\varepsilon_0}N_{\mathrm{d}}(E-E_{\mathrm{on,GB}})}\right)\left(1+\frac{1}{\alpha V_t}\sqrt{\frac{2q}{\varepsilon\varepsilon_0}N_{\mathrm{d}}(E-E_{\mathrm{on,GB}})}\right)} \tag{3}$$

Here k_{h} and k_{e} are effective rate constants that reflect the hole- and electron-induced surface activities, respectively; both also depend on the respective (fixed) probe concentrations, and also implicitly have contributions from charge transport efficiencies to the nanorod surface. A is the electrochemically active surface area of the nanorod. v_{c}, μ_{n}, and V_{t} are the majority carrier recombination velocity ($v_{\mathrm{c}}=3\,\mathrm{cm\,s^{-1}}$; Supplementary Fig. 14), electron mobility ($\mu_{\mathrm{n}}\approx10^{-4}\,\mathrm{cm^2\,V^{-1}\,s^{-1}}$)[55], and thermal voltage ($V_{\mathrm{t}}\approx0.026$ V), respectively. Global fitting of v_{AR}–E and v_{Rz}–E data with equations (2) and (3) gave k_{h}, k_{e} and $E_{\mathrm{on,GB}}$ for each spot of each nanorod where i–E data was also measured (Fig. 1l and m).

Photoelectrochemical deposition and characterization of catalysts. Individual spots of $\mathrm{TiO_2}$ nanorods were modified with a Co-$\mathrm{B_i}$ OEC[56] using a photoelectrochemical deposition method following previous studies of Co-based catalysts on metal oxide photoanodes[30,57–60]. Deaerated 1 M KCl, 100 mM sodium borate (pH 8.3) electrolyte containing 0.5 mM $\mathrm{CoCl_2}$ continuously flowed through the electrochemical cell while the potential was maintained at 0.0 V versus Ag/AgCl. Deposition occurred on specific locations of nanorods by focusing the 375-nm laser beam (552 kW cm^{-2}) onto a spot for 5 s (Extended Data Fig. 9a). A time-dependence experiment indicated that this deposition condition ensured that the photocurrent enhancement is saturated with the amount of deposited OEC (Extended Data Fig. 9b); this saturation behaviour is in agreement with the literature[4,26]. Consistently, the absorbed-photon-to-current efficiency η after OEC deposition is independent of the OEC coverage (Extended Data Fig. 9d). A representative optical transmission image of OEC-modified nanorods is shown in Extended Data Fig. 9a. The OEC appeared as a dark object on individual nanorods. The OEC coverage was estimated by analysing the SEM images of nanorods after OEC deposition (Supplementary Fig. 2). Here we first determined the bare nanorod structural contour in the SEM image. Then the area outside the contour and within the deposition laser focus was used as the measure for the amount of catalyst deposited in units of micrometres squared.

32. Xu, W., Jain, P. K., Beberwyck, B. J. & Alivisatos, A. P. Probing redox photocatalysis of trapped electrons and holes on single Sb-doped titania nanorod surfaces. *J. Am. Chem. Soc.* **134,** 3946–3949 (2012).
33. Chen, T.-Y. *et al.* Concentration and chromosome-organization dependent regulator unbinding from DNA for transcription regulation in living *Escherichia coli* cells. *Nature Commun.* **6,** 7445 (2015).
34. Sambur, J. B. & Chen, P. Approaches to single-nanoparticle catalysis. *Annu. Rev. Phys. Chem.* **65,** 395–422 (2014).
35. Byers, J. C., Güell, A. G. & Unwin, P. R. Nanoscale electrocatalysis: visualizing oxygen reduction at pristine, kinked, and oxidized sites on individual carbon nanotubes. *J. Am. Chem. Soc.* **136,** 11252–11255 (2014).
36. Chen, S. & Kucernak, A. Electrocatalysis under conditions of high mass transport rate: oxygen reduction on single submicrometer-sized Pt particles supported on carbon. *J. Phys. Chem. B* **108,** 3262–3276 (2004).
37. Meier, J., Friedrich, K. A. & Stimming, U. Novel method for the investigation of single nanoparticle reactivity. *Faraday Discuss.* **121,** 365–372 (2002).
38. Tel-Vered, R. & Bard, A. J. Generation and detection of single metal nanoparticles using scanning electrochemical microscopy techniques. *J. Phys. Chem. B* **110,** 25279–25287 (2006).
39. Ebejer, N., Schnippering, M., Colburn, A. W., Edwards, M. A. & Unwin, P. R. Localized high resolution electrochemistry and multifunctional imaging: scanning electrochemical cell microscopy. *Anal. Chem.* **82,** 9141–9145 (2010).
40. Li, Y., Cox, J. T. & Zhang, B. Electrochemical responses and electrocatalysis at single Au nanoparticles. *J. Am. Chem. Soc.* **132,** 3047–3054 (2010).
41. Xiao, X. & Bard, A. J. Observing single nanoparticle collisions at an ultramicroelectrode by electrocatalytic amplification. *J. Am. Chem. Soc.* **129,** 9610–9612 (2007).
42. Novo, C., Funston, A. M. & Mulvaney, P. Direct observation of chemical reactions on single gold nanocrystals using surface plasmon spectroscopy. *Nature Nanotechnol.* **3,** 598–602 (2008).
43. Shan, X. *et al.* Imaging the electrocatalytic activity of single nanoparticles. *Nature Nanotechnol.* **7,** 668–672 (2012).
44. Tang, M. L., Liu, N., Dionne, J. A. & Alivisatos, A. P. Observations of shape-dependent hydrogen uptake trajectories from single nanocrystals. *J. Am. Chem. Soc.* **133,** 13220–13223 (2011).
45. Plessers, E. *et al.* Resolving interparticle heterogeneities in composition and hydrogenation performance between individual supported silver on silica catalysts. *ACS Catal.* **5,** 6690–6695 (2015).
46. Xing, J. *et al.* Stable isolated metal atoms as active sites for photocatalytic hydrogen evolution. *Chem. Eur. J.* **20,** 2138–2144 (2014).
47. Ida, S., Kim, N., Ertekin, E., Takenaka, S. & Ishihara, T. Photocatalytic reaction centers in two-dimensional titanium oxide crystals. *J. Am. Chem. Soc.* **137,** 239–244 (2015).
48. Sze, S. M. *Semiconductor Devices, Physics and Technology* 3rd edn (Wiley, 2011).
49. Wang, Y., Warschkow, O. & Marks, L. D. Surface evolution of rutile $\mathrm{TiO_2}$ (100) in an oxidizing environment. *Surf. Sci.* **601,** 63–67 (2007).
50. Warschkow, O., Wang, Y., Subramanian, A., Asta, M. & Marks, L. D. Structure and local-equilibrium thermodynamics of the *c*(2 × 2) reconstruction of rutile $\mathrm{TiO_2}$ (100). *Phys. Rev. Lett.* **100,** 086102 (2008).
51. Lindquist, S. E., Finnström, B. & Tegnér, L. Photoelectrochemical properties of polycrystalline $\mathrm{TiO_2}$ thin film electrodes on quartz substrates. *J. Electrochem. Soc.* **130,** 351–358 (1983).
52. Fàbrega, C. *et al.* Tuning the Fermi level and the kinetics of surface states of $\mathrm{TiO_2}$ nanorods by means of ammonia treatments. *J. Phys. Chem. C* **117,** 20517–20524 (2013).
53. Peterson, M. W., Turner, J. A. & Nozik, A. J. Mechanistic studies of the photocatalytic behavior of titania: particles in a photoelectrochemical slurry cell and the relevance to photodetoxification reactions. *J. Phys. Chem.* **95,** 221–225 (1991).
54. Shen, H., Zhou, X., Zou, N. & Chen, P. Single-molecule kinetics reveals a hidden surface reaction intermediate in single-nanoparticle catalysis. *J. Phys. Chem. C* **118,** 26902–26911 (2014).
55. Chen, H., Wei, Z., Yan, K., Bai, Y. & Yang, S. Unveiling two electron-transport modes in oxygen-deficient $\mathrm{TiO_2}$ nanowires and their influence on photoelectrochemical operation. *J. Phys. Chem. Lett.* **5,** 2890–2896 (2014).
56. Surendranath, Y., Dincă, M. & Nocera, D. G. Electrolyte-dependent electrosynthesis and activity of cobalt-based water oxidation catalysts. *J. Am. Chem. Soc.* **131,** 2615–2620 (2009).
57. Zhong, D. K., Cornuz, M., Sivula, K., Gratzel, M. & Gamelin, D. R. Photo-assisted electrodeposition of cobalt-phosphate (Co-Pi) catalyst on hematite photoanodes for solar water oxidation. *Energy Environ. Sci.* **4,** 1759–1764 (2011).
58. Ye, H., Park, H. S. & Bard, A. J. Screening of electrocatalysts for photoelectrochemical water oxidation on W-doped $\mathrm{BiVO_4}$ photocatalysts by scanning electrochemical microscopy. *J. Phys. Chem. C* **115,** 12464–12470 (2011).
59. Abdi, F. F. & van de Krol, R. Nature and light dependence of bulk recombination in Co-Pi-catalyzed $\mathrm{BiVO_4}$ photoanodes. *J. Phys. Chem. C* **116,** 9398–9404 (2012).
60. Pilli, S. K. *et al.* Efficient photoelectrochemical water oxidation over cobalt-phosphate (Co-Pi) catalyst modified $\mathrm{BiVO_4}$/1D-$\mathrm{WO_3}$ heterojunction electrodes. *Phys. Chem. Chem. Phys.* **15,** 14723–14728 (2013).
61. Çakir, S. & Arslan, E. Voltammetry of resazurin at a mercury electrode. *Chem. Pap.* **64,** 386–394 (2010).

62. Cooper, G., Turner, J. A. & Nozik, A. J. Mott-Schottky plots and flatband potentials for single crystal rutile electrodes. *J. Electrochem. Soc.* **129,** 1973–1977 (1982).
63. Bolts, J. M. & Wrighton, M. S. Correlation of photocurrent-voltage curves with flat-band potential for stable photoelectrodes for the photoelectrolysis of water. *J. Phys. Chem.* **80,** 2641–2645 (1976).
64. Möllers, F., Tolle, H. J. & Memming, R. On the origin of the photocatalytic deposition of noble metals on TiO_2. *J. Electrochem. Soc.* **121,** 1160–1167 (1974).
65. Laser, D. & Gottesfeld, S. Photocurrents induced by subbandgap illumination in a Ti-oxide film electrode. *J. Electrochem. Soc.* **126,** 475–478 (1979).
66. Abrantes, L. M. & Peter, L. M. Transient photocurrents at passive iron electrodes. *J. Electroanal. Chem. Interf. Electrochem.* **150,** 593–601 (1983).
67. Peter, L. M. Dynamic aspects of semiconductor photoelectrochemistry. *Chem. Rev.* **90,** 753–769 (1990).
68. Zhang, Q. *et al.* Density of deep trap states in oriented TiO_2 nanotube arrays. *J. Phys. Chem. C* **118,** 18207–18213 (2014).
69. Sagara, T. & Sukigara, M. Photogenerated surface states at n-TiO_2 / aqueous solution interface. *J. Electrochem. Soc.* **135,** 363–367 (1988).
70. Tafalla, D., Pujadas, M. & Salvador, P. Direct measurements of flat-band potential shifts under illumination of the semiconductor-electrolyte interface by electrolyte electroreflectance. *Surf. Sci.* **215,** 190–200 (1989).

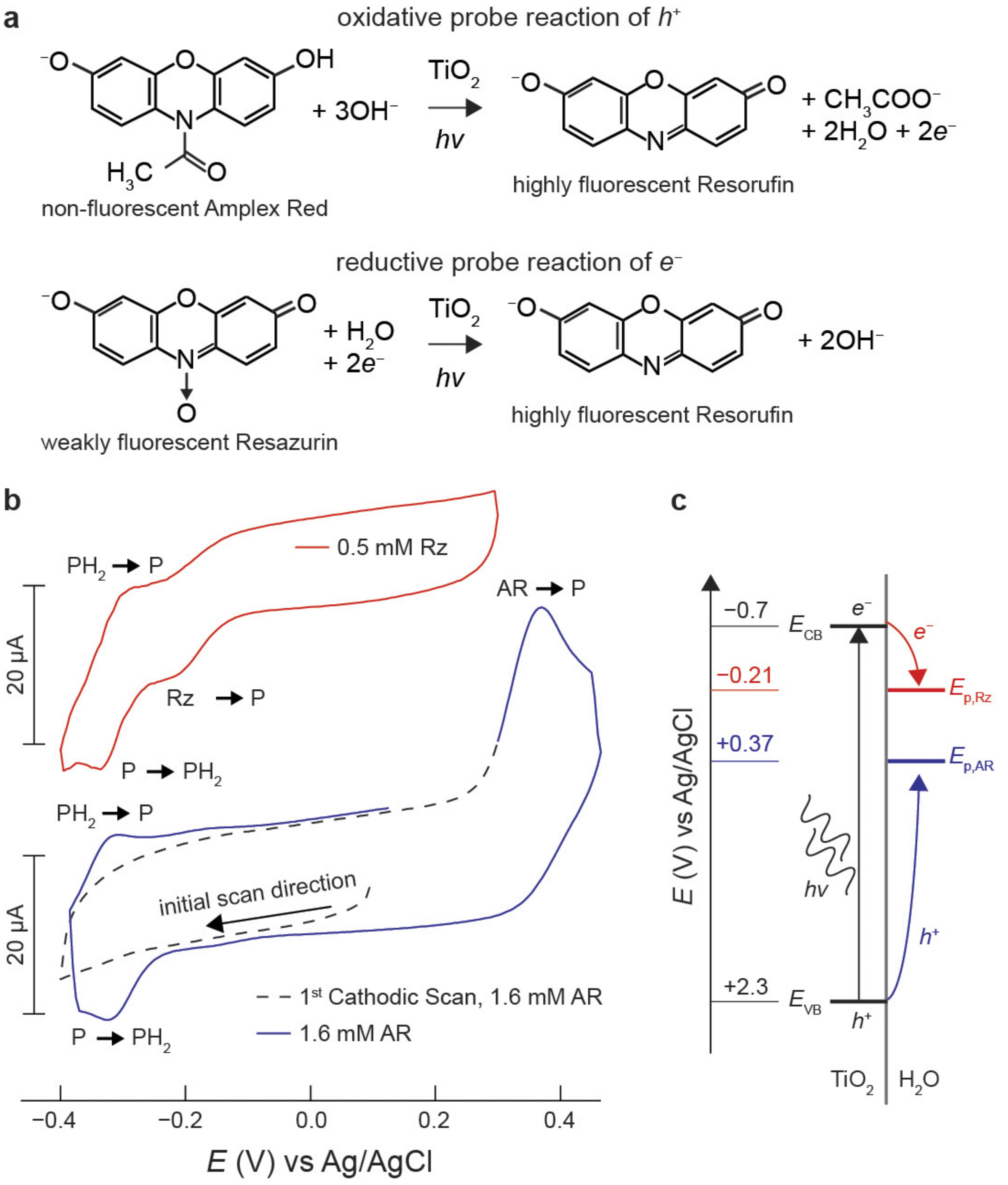

Extended Data Figure 1 | Carrier-selective fluorogenic probe reactions, and electrochemistry and energy-level alignment of the probe molecule redox potentials relative to TiO_2 band edges. a, The oxidative N-deacetylation of amplex red to resorufin probes photogenerated holes (or consequent oxidizing species, such as surface-adsorbed hydroxyl radicals, $OH^\bullet$ radicals) and the reductive N-deoxygenation of resazurin to resorufin probes photogenerated electrons. **b**, Cyclic voltammetry of 0.5 mM resazurin (Rz, red trace) and 1.6 mM amplex red (AR, black and blue traces) in N_2-purged electrolyte. Scan rate is $2\,\mathrm{mV\,s^{-1}}$ and the working electrode is glassy carbon. The irreversible reduction wave with a peak potential $E_{\mathrm{p,Rz}} = -0.21$ V is due to the reduction of resazurin to resorufin (product P)[13,61]. The reversible redox waves with a half-wave potential $E_{1/2} = -0.32$ V are from the resorufin/dihydroresorufin redox couple (that is, resorufin/PH_2)[13,61]. The irreversible oxidation wave was assigned to the irreversible oxidation of amplex red to resorufin, with a peak potential $E_{\mathrm{p,AR}} = +0.37$ V. **c**, Energy-level diagram of the peak potentials of resazurin reduction ($E_{\mathrm{p,Rz}}$) and amplex red ($E_{\mathrm{p,AR}}$) oxidation relative to the conduction (E_{CB}) and valence band (E_{VB}) edges of bulk TiO_2. The blue and red arrows schematically illustrate the energetically possible pathways of photogenerated holes and electrons to amplex red and resazurin, respectively. *hv* indicates incident light.

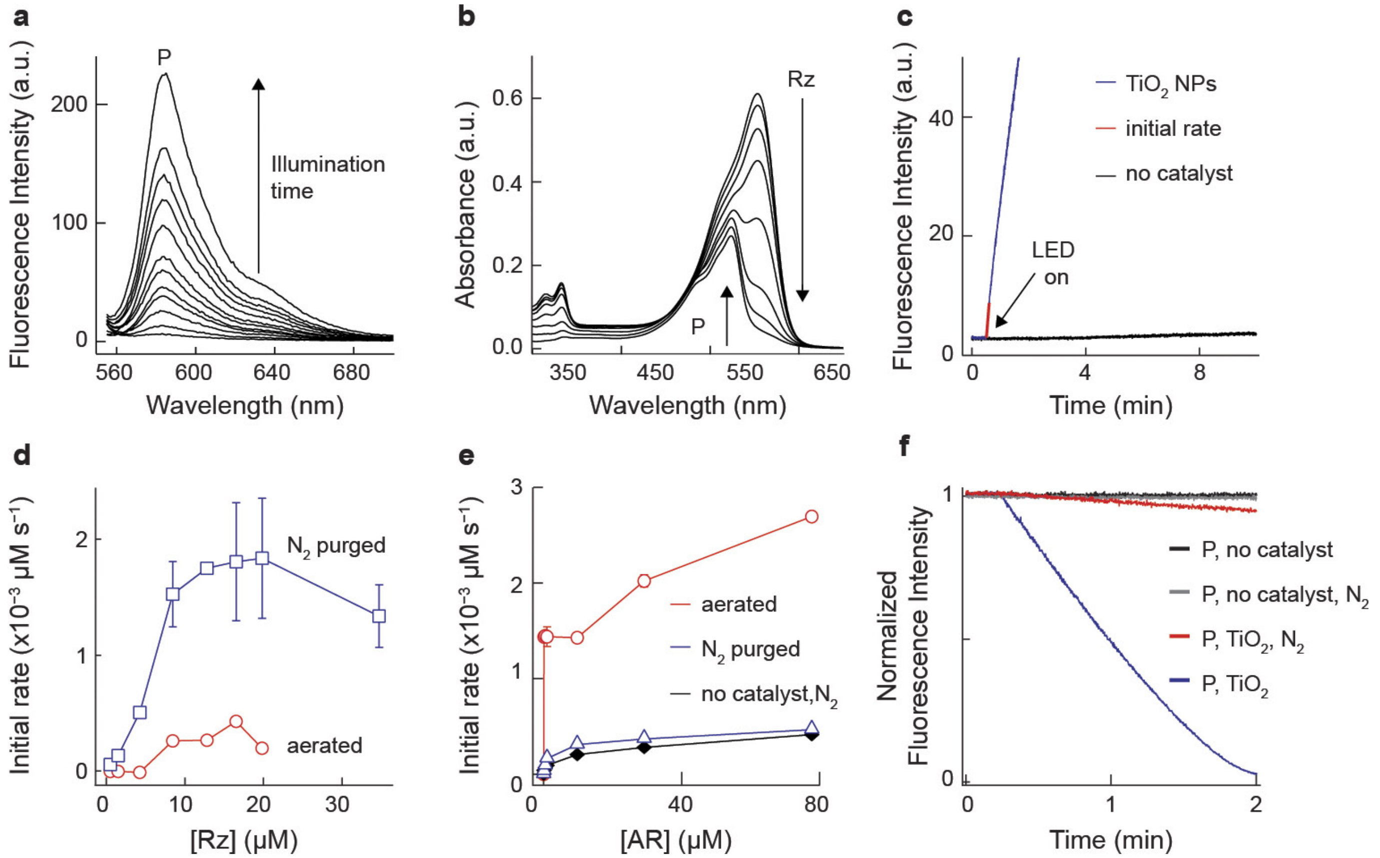

Extended Data Figure 2 | TiO$_2$ nanoparticles photocatalytically oxidize amplex red and reduce resazurin to generate resorufin. Ensemble-level photocatalysis experiments were performed using P25 titanium dioxide nanoparticles, the precursor material for TiO$_2$ nanorods, because they were easily dispersed in aqueous solution. The nanorods were easily dispersed in ethanol–water mixtures, but this solvent is not ideal for studying amplex red oxidation because ethanol could preferentially react with photogenerated holes. **a** and **b**, Fluorescence and ultraviolet–visible absorption spectroscopy confirm the generation of resorufin from amplex red oxidation (**a**) or resazurin reduction (**b**) photo-catalysed by TiO$_2$ nanoparticles. **a**, Fluorescence spectra of a 10-µM amplex red solution in an aerated pH 8.3 electrolyte as a function of 365-nm LED illumination time (45 mW cm^{-2}). **b**, Ultraviolet–visible absorption spectra of a 10-µM resazurin solution in N$_2$-purged pH 8.3 electrolyte as a function of illumination time; no isosbestic point is observed in the data, suggesting that resorufin is further consumed in the photocatalytic reaction. **c**–**e**, Photocatalytic kinetics of resazurin reduction (**c**, **d**) and amplex red oxidation (**e**) as a function of electrolyte composition. **c**, Fluorescence intensity at 585 nm versus time data used to determine the initial rate from a linear fit of the data after the 365 nm LED light is turned on (red line) for photocatalytic reduction of resazurin. The arbitrary fluorescence units were converted into concentration units by making a calibration curve using serial dilution of resorufin standards. NPs are nanoparticles. **d**, Initial rate of resazurin reduction versus bulk resazurin concentration at a fixed light intensity in aerated (red open circles) and N$_2$-purged (blue open squares) electrolyte. The initial rate saturates with increasing resazurin concentration, [Rz], which suggests that the reaction occurs on the catalyst surface and the number of available surface sites on the catalyst limits the initial reaction rate at high concentrations of the reactant resazurin. **e**, Initial rate of amplex red oxidation versus bulk amplex red concentration, [AR], in aerated (red open circles) and N$_2$-purged (blue open triangles) electrolyte. A control experiment without catalyst is also shown (black filled diamonds). In N$_2$-purged electrolyte the initial amplex red rate also exhibits saturation kinetics with increasing [AR], but the saturation level is much lower than that in aerated solution. This lower-saturation oxidation rate may be due to the removal of the possible O$_2^{-\bullet}$-induced amplex red oxidation channel or electron accumulation in TiO$_2$ particles in the absence of electron acceptors in the solution (for example, dissolved O$_2$), which will not occur in photoelectrocatalysis experiments because electrons will be collected by the working electrode. The autocatalytic amplex red conversion to resorufin under ultraviolet illumination does not contribute much to our single-molecule imaging results of photoelectrocatalytic oxidation of amplex red on TiO$_2$ because the process occurs predominantly in the bulk solution rather than on the surface of TiO$_2$ and would not depend on the electrode potential. **f**, Decomposition of resorufin by TiO$_2$ nanoparticles in aerated (blue line) and N$_2$-purged electrolyte (red line). This process could contribute to the short resorufin residence time on the TiO$_2$ surface (Extended Data Fig. 7). The rate of resorufin decomposition is accelerated in aerated electrolyte, similar to amplex red, which suggests an oxidative pathway for the decomposition of resorufin. The black and grey lines are controls. The reaction volume in each experiment was 2 ml, into which 100 µl of a 1 mg ml^{-1} aqueous solution of P25 nanoparticles was added.

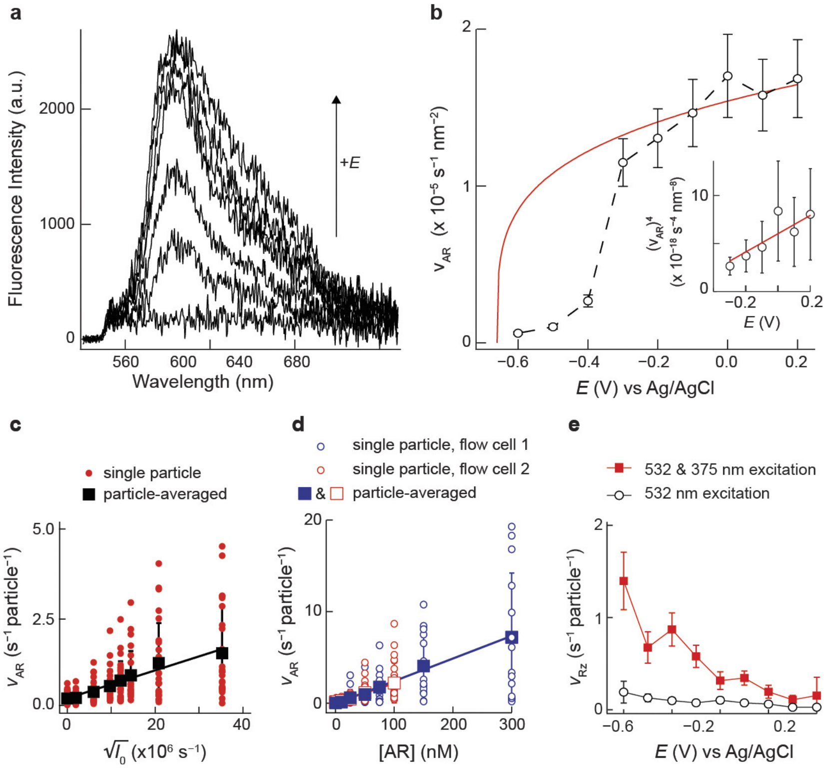

Extended Data Figure 3 | TiO_2 nanorods photoelectrocatalytically oxidize amplex red and reduce resazurin to generate resorufin. **a**–**d**, ν_{AR} scales with $E^{1/4}$ for $E \geq -0.3$ V, with $I_0^{1/2}$ at fixed positive E, and also scales with [AR] at fixed E and I_0. **a**, A series of fluorescence spectra measured from a single TiO_2 nanorod on ITO as a function of applied potential from −0.6 V to +0.0 V in N_2-purged electrolyte with 50 nM amplex red under 375-nm laser illumination of 60 W cm^{-2} and 532-nm laser illumination of 630 W cm^{-2}. Each spectrum was acquired for 5 s, and it shows the characteristic fluorescence spectrum of resorufin. **b**, Single-molecule amplex red oxidation rate (ν_{AR}) averaged over the 37 nanorods used in the study. The red line represents a fit to the data with equation (2) in the main text to illustrate the rate dependence on the applied potential (an ensemble-averaged $E_{on,GB} = -0.64$ V was obtained here). Only the data more positive than −0.3 V were fitted, for the reasons discussed in Extended Data Fig. 4b caption. The error bars represent s.e.m. The inset plots ν_{AR}^4 versus E to show the linear behaviour at E more positive than −0.3 V. **c**, Amplex red oxidation rate per particle versus the square root of incident light power in the presence of 50-nM bulk [AR] and +0.2 V, demonstrating that ν_{AR} scales with $I_0^{1/2}$ at a fixed positive E. The red dots indicate data from individual particles and the black squares represent the average (error bars represent s.d.). **d**, At +0.2 V and 0.66-mW, 375-nm illumination (the highest light power in **c**) the reaction rate was observed to increase linearly with bulk [AR]. Two sets of data were included from two different flow cells, where the dots indicate individual particles and the solid squares represent the average (error bars are s.d.). Therefore, under our experimental single-molecule imaging conditions, the reaction rate is in the linear range in its dependence on [AR]. **e**, Resazurin is dominantly reduced by photogenerated conduction band electrons. Single-particle, single-molecule data of resazurin reduction averaged over a large number of TiO_2 nanorods in N_2-purged electrolyte contained 50 nM resazurin. The control (black circles) without 0.66-mW, 375-nm laser illumination is also shown. The difference here demonstrates that resazurin is dominantly reduced by photogenerated conduction band electrons, while resazurin reduction under dark is negligible.

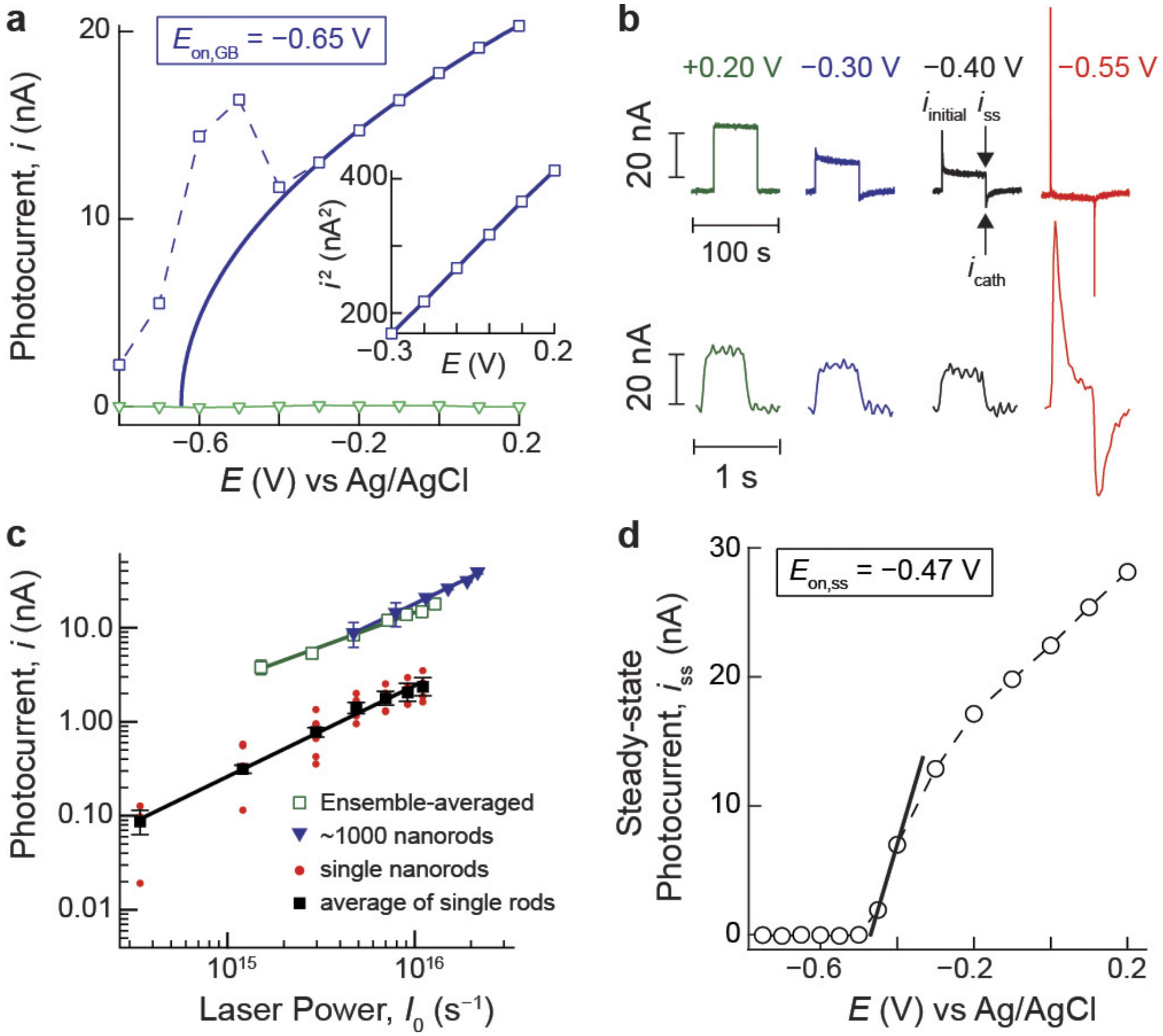

Extended Data Figure 4 | Photoelectrochemical water oxidation properties of TiO_2 nanorods. i scales with $E^{1/2}$ for $E \geq -0.3$ V and with I_0 at fixed E, and determination of $E_{on,ss}$. **a**, i–E data of ~1,000 nanorods measured with lock-in detection method using 1-Hz chopped 20-mW, 532-nm light illumination (green triangles) and 12-mW, 375-nm laser illumination (blue squares) in the TIRF geometry, demonstrating that anodic photocurrent was only observed under band gap illumination with the 375-nm laser. The solid line is a fit to the data at $E \geq -0.3$ V with equation (1) in the main text to yield $E_{on,GB} = -0.65$ V. This $E_{on,GB}$ value agrees with the photocurrent onset potential determined for bulk rutile TiO_2, which is also nearly equivalent to the flat band potential determined under dark conditions[62,63]. The inset shows that i^2 scales linearly with E at $E \geq -0.3$ V. For $E < -0.3$ V, the photocurrent deviates from the $E^{1/2}$ dependence owing to photocurrent transient dynamics (see **b**), which have been previously observed and described in detail[19,29,64–68]. **b**, Representative photocurrent–time (i–t) responses over a range of potentials during a single on-off cycle at 10 mHz (top) or 1 Hz (bottom) light chopping (50% duty cycle) to mimic steady-state single-molecule imaging and single-nanorod photocurrent measurement conditions, respectively. The background dark current measured from the macroscopic ITO electrode was subtracted using a two-point linear background subtraction method to an average of five consecutive data points before and after illumination. Data was collected with 20-ms time resolution. Three distinct features are clear (denoted on the −0.4-V data; black trace): (1) an initial photocurrent spike ($i_{initial}$) when the light is turned on, (2) a decay of the photocurrent on a millisecond-to-second timescale while the light is on towards a steady-state current (i_{ss}), and (3) an initial negative, cathodic photocurrent spike (i_{cath}) when the illumination is turned off, which decays to the background current level also on a millisecond-to-second timescale. When the photocurrent transient behaviour dominates the i–t response at $E < -0.3$ V, the photocurrent signal measured by the lock-in amplifier is somewhere between the initial photocurrent spike ($i_{initial}$) and steady-state photocurrent (i_{ss}), which is expected because the lock-in detection is dependent on the signal shape versus time. Following references 19 and 69, we fit i–E data for $E \geq -0.3$ V in **a**. **c**, Photocurrent versus 375-nm laser power I_0 at +0.2 V for three different illumination conditions, demonstrating that at fixed positive potentials, i scales linearly with I_0 over a broad range of power densities (milliwatts to megawatts per centimetre squared). The geometric spot size of the laser spot was (1) 1×1 cm^2 for ensemble-averaged measurements (open green squares, spanning a power density range of 0.8–6.8 mW cm^{-2}), (2) 80×95 μm^2 to excite ~1,000 nanorods in the TIRF geometry (solid blue triangles, spanning a power density range of 32.9–151.3 W cm^{-2}), and (3) 390×390 nm^2 for single-nanorod measurements (solid red circles, spanning a power density range of 0.1–6.6 MW cm^{-2}). **d**, Steady-state photocurrent i_{ss}–E data (black circles, same data as included in Fig. 1n) obtained from 10-mHz chopped-light illumination experiments. The steady-state photocurrent onset potential ($E_{on,ss}$) is defined as the intersection point of zero photocurrent and the tangent at maximum slope of photocurrent[57]. The solid black line indicates the linear fit to determine $E_{on,ss} = -0.47$ V. This $E_{on,ss}$ value is ~200 mV more positive than the $E_{on,GB}$ value (−0.65 V) in **a**; this difference has been previously observed and attributed to surface charging[19,70]. Despite the difference in their absolute values, the relative values and variations of $E_{on,GB}$ among individual nanorod spots are good reflections of the relative values and variations of their $E_{on,ss}$, as $E_{on,GB}$ is linearly correlated with $E_{on,ss}$ (see Supplementary Fig. 20b in Supplementary Note 5.4).

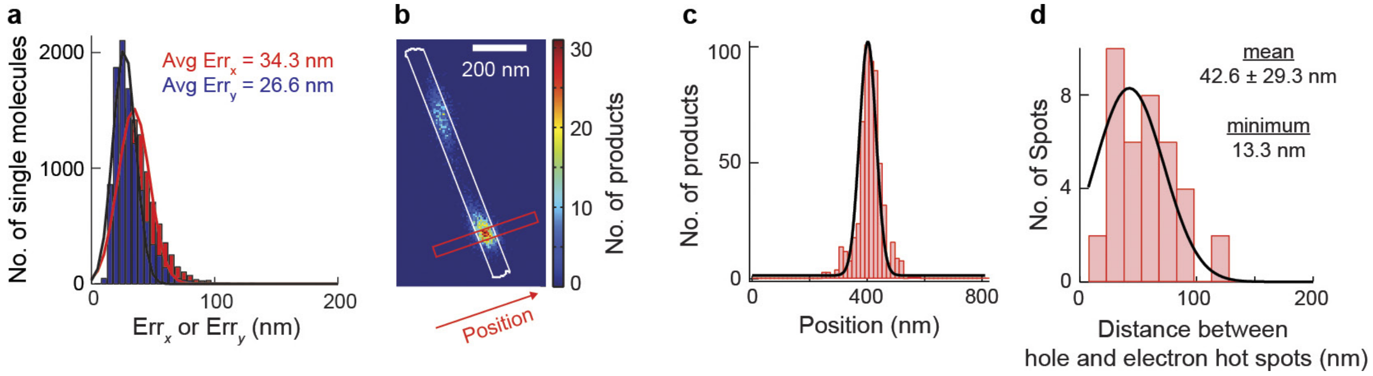

Extended Data Figure 5 | Product localization accuracy, hotspot size, as well as position correlation of hole- and electron-induced reaction hotspots. a, Localization precision of product molecule positions. Distribution of the error in x and y (that is, Err$_x$ or Err$_y$) for all single molecules detected on the surface of a single nanorod, calculated using Supplementary equation (3). The average errors were determined with a one-dimensional Gaussian fit (solid lines). **b**–**d**, Size of localized reaction hotspots, and distribution of distances between corresponding high-reaction-rate electron and hole hotspots. **b**, Two-dimensional histogram ($15 \times 15\,\mathrm{nm}^2$ bins) of all hole-induced reaction product positions over the potential range $E = -0.6$ V to $+0.2$ V of a single nanorod exhibiting a localized, hole activity hotspot. The red rectangular area represents the region where a one-dimensional histogram was plotted in **c**. **c**, One-dimensional histogram from the region in **b**. The solid line is a Gaussian fit. The full-width at half-maximum (FWHM), which is used as a measure of this hotspot size, is 52 nm, much smaller than the diffraction-limited resolution of ~300 nm. **d**, Distributions of distances between corresponding hole and electron reaction hotspots on individual nanorods. Each hotspot's centre position was determined by two-dimensional Gaussian fitting to two-dimensional reaction product histograms. The average distance between localized hole and electron hot-spots is ~42 nm, and the minimum distance is ~13 nm.

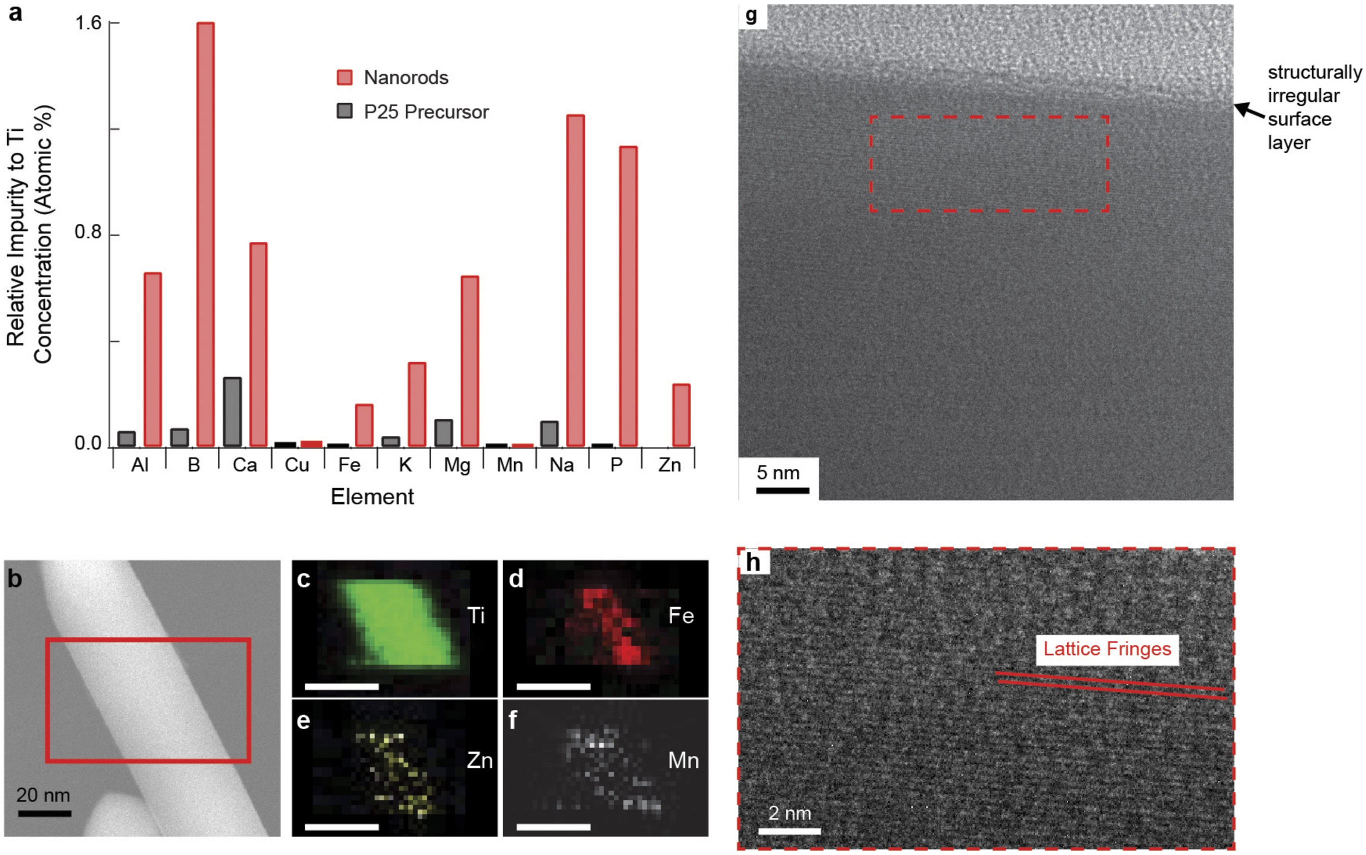

Extended Data Figure 6 | Elemental analysis and high-resolution electron microscopy for identifying possible active sites on these TiO_2 nanorods. See Methods for more details. **a**, Atomic concentration of impurity elements relative to Ti measured via ICP-AES in commercial P25 nanoparticles (black bars, precursor used in the synthesis) and the as-synthesized TiO_2 nanorod sample (red bars). The dried powder samples were digested in 1 ml each of hot, concentrated HNO_3 and HCl and submitted for elemental analysis at the Cornell Nutrient Analysis Laboratory. The total amount of TiO_2 dissolved in the acid digestion process was difficult to quantify, so the concentration of impurity elements in each sample were calculated relative to the total amount of Ti detected. The ICP-AES data suggests that substantial concentration increases in elements such as Al, B, Ca, Fe, K and Mg, as well as the introduction of Zn, are due to impurity incorporation during the high-temperature synthetic method, probably from reagent impurities (for example, in reagent-grade NaCl and Na_2HPO_4). This hypothesis is further supported by ref. 14, which demonstrated that eight different transition metals (including Fe) could be substitutionally doped for Ti at an atomic concentration of 2%. **b**, High-angle annular dark field scanning TEM (HAADF-STEM) image of a single nanorod. The red box indicates a region of the image where energy-dispersive X-ray analysis was performed. **c**–**f**, Energy-dispersive X-ray analysis mapping of Ti and other detected impurity elements revealed a heterogeneous distribution of impurities: Fe (**d**), Zn (**e**) and Mn (**f**). **g**, High-resolution bright field TEM image of a single nanorod shows structural irregularities along the side surfaces. **h**, Zoomed-in view from the dashed red box in **g** shows lattice fringes, evidence that each rod is a single crystal. Similar lattice fringes were also observed by ref. 14.

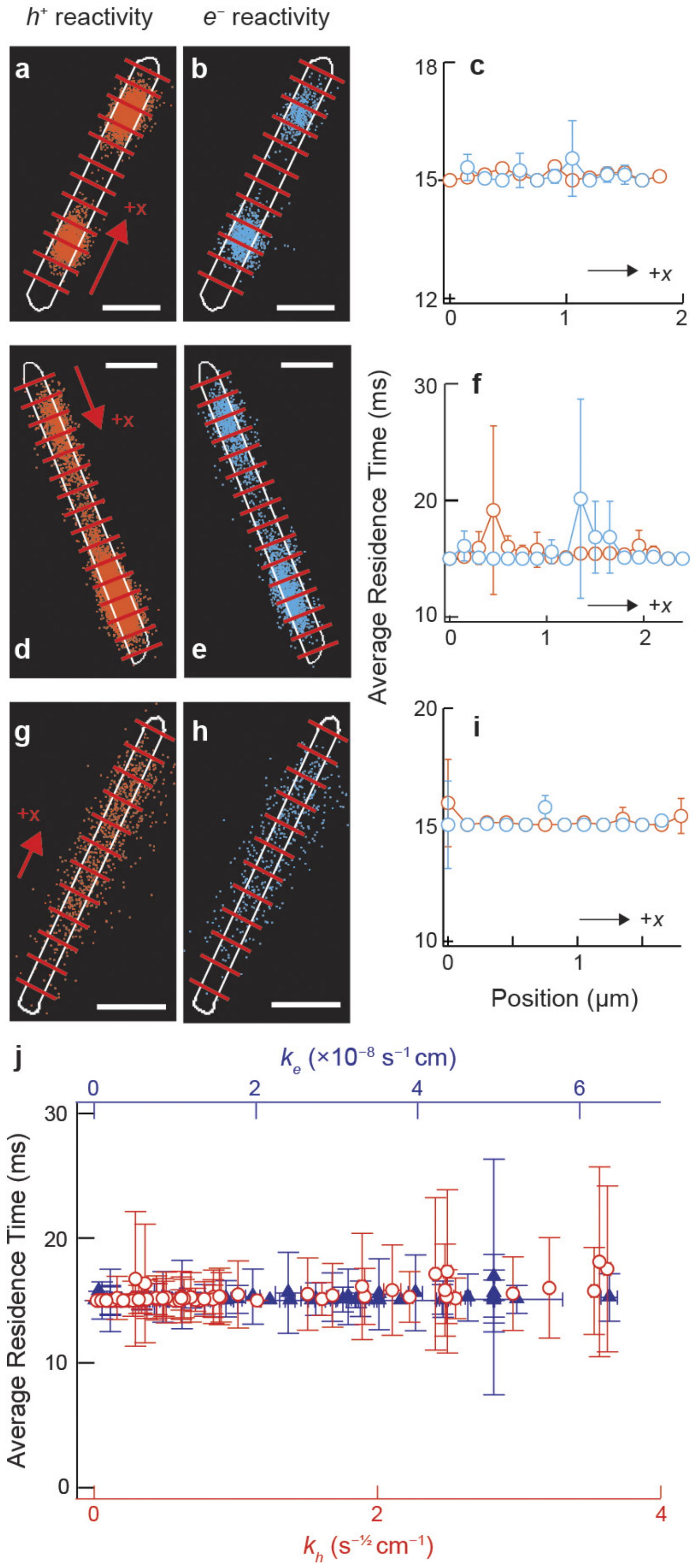

Extended Data Figure 7 | The two structurally similar probe molecules amplex red and resazurin adsorb to all surface sites equivalently. See Methods for more details. **a**, **b**, **d**, **e**, **g**, **h**, Scatter plots of all individual resorufin molecules generated from (**a**, **d** and **g**) hole-induced amplex red oxidation (orange dots) and (**b**, **e** and **h**) electron-induced resazurin reduction reactions (blue dots) on the same three TiO_2 nanorods shown in Fig. 1. The red lines dissect each nanorod into 150-nm segments along its length, within each of which the average residence time is calculated. **c**, **f** and **i**, Average product residence time versus position along the nanorod for hole-induced amplex red oxidation (orange circles) and electron-induced resazurin reduction (blue circles) reactions. **j**, Average product residence time formed from hole-induced amplex red oxidation (red circles) and electron-induced resazurin reduction (blue diamonds) reactions plotted versus the corresponding k_h and k_e values for all 78 nanorod spots studied herein. The error bars represent s.d.

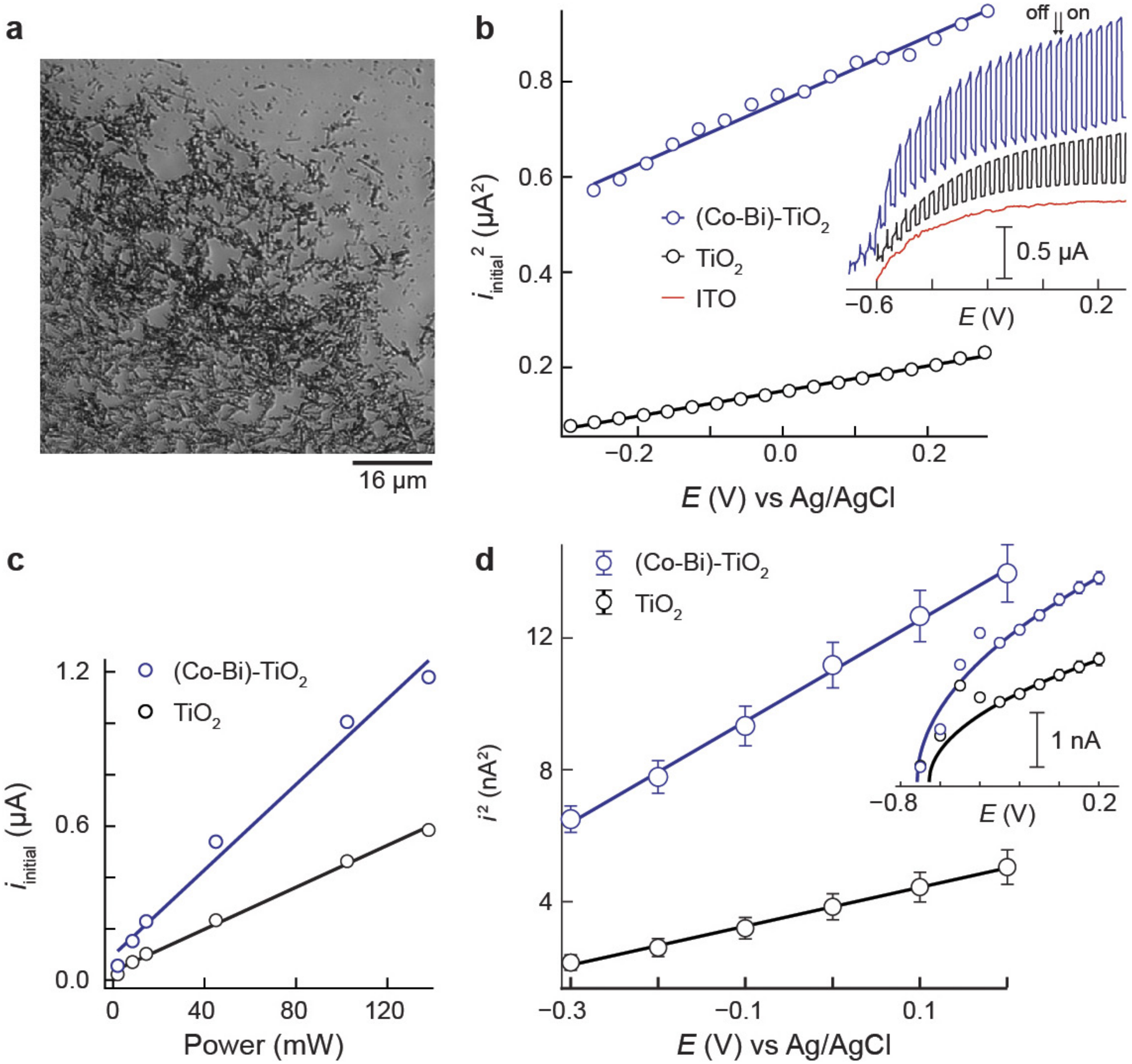

Extended Data Figure 8 | Photoelectrochemical properties of bare and (Co-B$_i$) modified TiO$_2$ nanorods. a–**c**, Ensemble-level i–E and i–I_0 data of bare and (Co-B$_i$)-modified TiO$_2$ nanorod thin films. **a**, Representative optical transmission image of a thin film of TiO$_2$ nanorods on an ITO electrode. **b**, i^2 is linearly proportional to E for the same bare (black circles) and OEC-modified thin film sample as in **a** at $E \geq -0.3$ V. Data were obtained from chopped light (138 mW cm^{-2}, 365 nm LED) linear sweep voltammograms (−10 mV s^{-1} from +0.3 V, see inset) for a bare ITO electrode (red trace), TiO$_2$ nanorod-coated thin film electrode (black trace) and (Co-B$_i$)-TiO$_2$ electrode in N$_2$-purged electrolyte (blue trace). The data have been slightly offset for clarity. Co-B$_i$ OEC was photoelectrochemically deposited from electrolyte containing 0.5 mM CoCl$_2$ at 0.0 V for 30 min using 365-nm LED illumination at 45 mW cm^{-2}. **c**, Photocurrent is linearly proportional to 365-nm light power at +0.3 V for the same TiO$_2$ (red circles) and (Co-B$_i$)-TiO$_2$ (blue circles) thin film sample in N$_2$-purged electrolyte. **d**, Single-nanorod averaged i^2 data are linearly proportional to E for bare (black circles) and Co-B$_i$ OEC modified (red circles) TiO$_2$ nanorods at $E \geq -0.3$ V. The data represents the average photocurrent of 78 nanorod spots from 37 individual nanorods and the error bars represent the standard error of the mean. The inset shows i–E response obtained by lock-in detection under 1-Hz illumination at the highest power density (6.6 mW cm^{-2}). The η and $E_{on,GB}$ obtained from fitting the data (lines) with equation (1) in the main text are $\eta = (5.72 \pm 0.11) \times 10^{-2}\%$ and $E_{on,GB} = -0.66 \pm 0.02$ V for TiO$_2$; and $\eta = (9.62 \pm 0.17) \times 10^{-2}\%$ and $E_{on,GB} = -0.72 \pm 0.02$ V for (Co-B$_i$)-TiO$_2$. Together, these data demonstrate that the i–$E^{1/2}$ (at $E \geq -0.3$ V) and i–I_0 scaling laws hold for both bare and OEC-modified nanorods, and in all cases, the photocurrent for the OEC-modified TiO$_2$ nanorod-coated electrode is higher than the bare TiO$_2$ nanorod-coated electrode. The OEC-induced photocurrent enhancement is also not due to larger photocurrent transient dynamics (Supplementary Note 5.7).

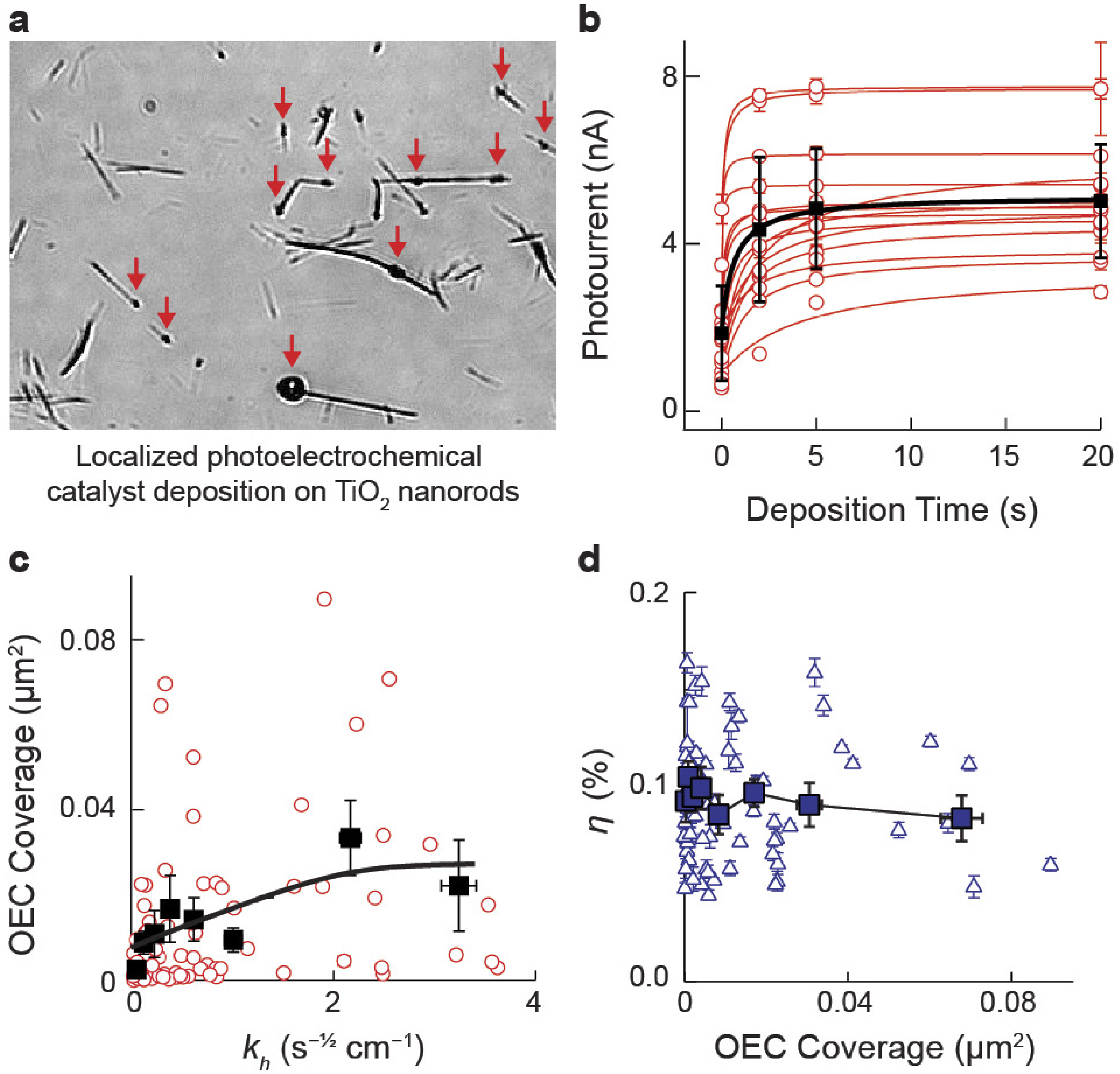

Extended Data Figure 9 | Developing a Co-B$_i$ OEC deposition method on single nanorods that produces a saturated photocurrent enhancement. **a**, Representative optical transmission image of a nanorod sample after localized photoelectrochemical deposition of Co-B$_i$ catalysts after 20 s deposition time. The red arrows indicate the location on which the focused laser was positioned for guided catalyst deposition, where the deposited catalysts appear as dark spots. **b**, Photocurrent at +0.2 V versus photoelectrochemical deposition time of the catalyst for single nanorods (red circles) and nanorod-averaged results (black squares). This photocurrent shows a saturation behaviour versus OEC deposition time (and hence OEC deposition amount), which was also observed for planar Fe$_2$O$_3$ thin films modified with a Co-phosphate catalyst[4,26]. Error bars represent s.d. In all of our single-nanorod OEC deposition studies presented in the main text, we used an OEC deposition time of 5 s at which, according to **b**, the photocurrent enhancement is already saturated. Thus, the η parameter obtained from fitting the i–E data of OEC-modified nanorod spots represents the maximum achievable η per spot, as well as the maximum achievable change in η (that is, $\Delta\eta$) between the same bare and OEC-modified nanorod spot. **c**, Catalyst coverage versus k_h (see Supplementary Fig. 2 for details on catalyst coverage quantification), demonstrating that more catalyst material is deposited onto higher-activity sites. The red circles represent data from individual nanorods and the black squares represent averaged data grouped by ten data points sorted by k_h. The same panel is also presented as Fig. 3c in the main text. **d**, η for OEC-modified nanorod spots versus catalyst coverage. η is essentially independent of OEC coverage, consistent with the saturated photocurrent behaviour in **b**. Filled squares represent data grouped by ten data points sorted by their catalyst coverage values. The error bars for all individual spot values represent s.d. The error bars in **c** and **d** for all binned data represent s.e.m.

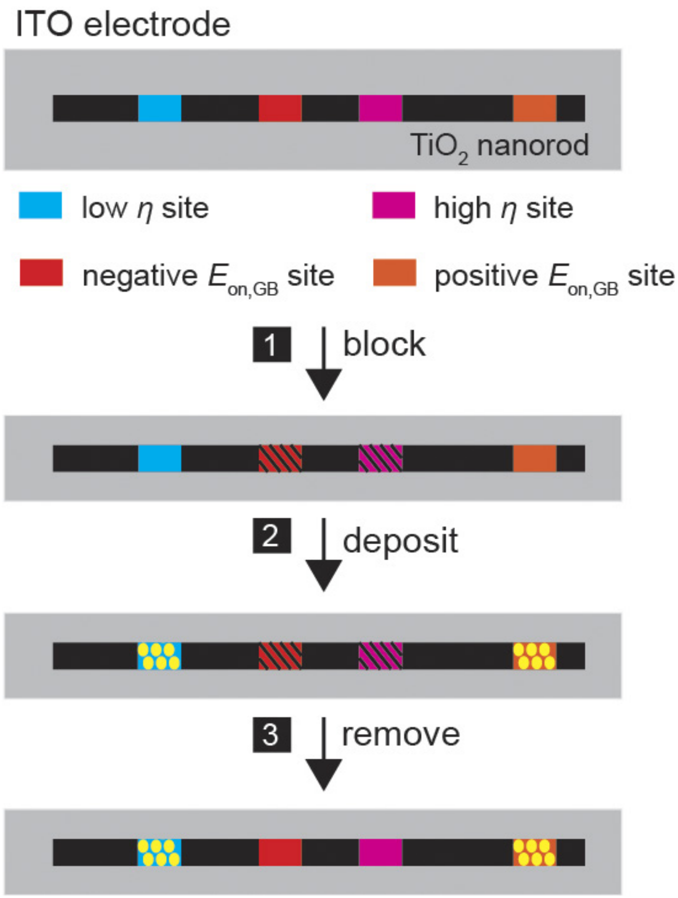

Extended Data Figure 10 | Proposed block–deposit–remove strategy, which has the potential to selectively deposit a desired OEC on low-activity and positive onset potential sites. First, a removable protective group can be photoelectrochemically deposited starting from negative potentials to block negative $E_{on,GB}$ sites. To block high-activity sites with similar $E_{on,GB}$ values, we propose that using short light pulses may cause more protecting group material to be deposited at higher-activity sites first. In this way, low η and positive $E_{on,GB}$ sites will remain unblocked. The potential could then be stepped from negative E to the ensemble-averaged steady-state photocurrent onset value, for example, and thus all remaining sites with $E_{on,GB}$ values more positive than the ensemble-averaged value will also remain unblocked. Second, the potential can be set to a positive value and a long light pulse can be used to deposit the desired OEC on all remaining sites: those with positive $E_{on,GB}$ and low η. Finally, the protective group can be subsequently removed to yield a photoanode with optimally located OECs. Yellow dots represent the OEC.